May 2018

Angularly Resolved Deep Brain Fluorescence Imaging Using a Single Optical Fiber

Israel Delarosa
University of Wisconsin-Milwaukee

ANGULARLY RESOLVED DEEP BRAIN FLUORESCENCE IMAGING USING A SINGLE OPTICAL FIBER

by

Israel Delarosa

A Thesis Submitted in

Partial Fulfillment of the

Requirements for the Degree of

Master of Science

in Engineering

at

The University of Wisconsin-Milwaukee

May 2018

ABSTRACT

ANGULARLY RESOLVED DEEP BRAIN FLUORESCENCE IMAGING
USING A SINGLE OPTICAL FIBER
by

Israel Delarosa

The University of Wisconsin-Milwaukee, 2018
Under the Supervision of Professor Ramin Pashaie

To further understand neural disorders as well as recognize complexities of normal brain functionality continuously drives the development and implementation of new research instruments and techniques. In neuroscience research one difficulty that these instruments face is accessing subcortical regions with minimal invasiveness. While electrode based deep brain stimulation (DBS) has been a primary technique in research it has also become an accepted alleviation method for some neurological diseases such as Parkinson's, epilepsy, and depression in severe cases. However, there are possible side effects that may arise from the lack of cell targeting in electrical stimulation.

Optogenetics, uses proteins from microbial opsins to make cell populations of interest sensitive to light exposure. These proteins allow us to use light of appropriate wavelengths to manipulate the activity of targeted neurons when successfully expressed. In optogentic practice target cells are also co-expressed with fluorescence bio-markers in order to evaluate the level of light sensitivity in the cells population of interest. Detection and imaging of these fluorescence

molecules have motivated the development of new devices however, there is still a limitation on these instruments for deep brain fluorescence imaging including the limitations on invasiveness, resolution, and penetration depth.

This project strives to address the need for the development of a practical and cost-efficient device to find the location of maximum light sensitivity and measure the spatial distribution of fluorescence molecules in deep brain regions. This goal is achieved by proposing a novel optoelectronic design that uses only a relatively thin (200um) penetrating and rotating side-firing fiber to scan the brain tissue and collect data sets. These data sets are processed in a computer to reconstruct images displaying the distribution of fluorescence molecules in a cylindrical volume surrounding the fiber. The main benefits of this design are the simplicity of the hardware and experimental protocols since the procedure is only minimally invasive and image development is performed by computer algorithms and image reconstruction subroutines.

To my parents, Celita and Fortunato

and my brother and sisters.

TABLE OF CONTENTS

LIST OF FIGURES

LIST OF ABBREVIATIONS

ChR2	Channelrhodopsin-2
DBS	Deep Brain Stimulation
EEDM	Excitation and Emission Detection Module
FWHM	Full-width at half maximum
GFP	Green Fluorescence Protein
MC	Monte Carlo
NpHR	Natronomonas Halorhodopsin
NA	Numerical Aperture
RTE	Radiative Transport Equation
YFP	Yellow Fluorescence Protein

ACKNOWLEDGEMENTS

I would like to recognize everyone who has helped me throughout my Master's Degree. I would like to express appreciation to my colleagues and current and past lab mates in the BIST lab. I specifically want to thank Mehdi who worked with me in the beginning of the project and who helped with the Monte Carlo simulations. Also, Farid and Rex who continuously discussed and challenged me about my project but also who shared with me their personal experiences with graduate school and who have extended to me their friendship.

I would like to thank my advisor Dr. Ramin Pashaie, for his words of encouragement and inspiration. In good and challenging moments, he helped me look ahead, towards resolution and/or growth. His valuable insight and his advice which extends well beyond this project motivates me to become the best engineer that I can be.

I would like to extend my gratitude to my committee members Dr. Chiu Tai Law and Dr. Yongjin Sung for agreeing to be part of the review committee. I would also like to thank our collaborators Dr. Fred Helmstetter and Dr. Patrick Cullen, from UW-Milwaukee Neuroscience Department for providing help with in-vivo experiments. Their partnerships have helped make this project possible.

Finally, I would like to thank my family and friends. I specially want to thank my parents, brother and sisters for their unconditional love and their heartening words toward me. They have always been proud of me and will always be the reason I want to make a difference in the world. My favorite friend Elijah whose sense of wonder and curiosity is an inspiration and encouragement and who has brought joy to all those around him.

Chapter 1. Introduction and Background

1.1 Introduction

While some fluorescence imaging/microscopy devices are no-invasive, they can only provide information about the brain close to the surface (<1mm). However, devices for fluorescence imaging of subcortical regions are quite invasive and costly. Imaging structural changes and functionality in specific brain regions due to changes in fluorescence can provide researchers with information necessary for diagnosis and treatment of diseases that have native impact on the region of interest. In brain studies, as in optogentics, finding the precise location of maximum light sensitivity for effective light stimulation delivery and visualizing the spatial distribution of fluorescence molecules in deep brain regions presents challenges in the amount of invasiveness, light penetration depth, and spatial resolution.

Light penetration depth and spatial resolution of fluorescence imaging is affected by distinctions in the wavelength dependent optical properties of tissue including the scattering and absorption coefficients. The penetration ability of light to interact with tissue components and travel though this tissue until detection, is imperative to diagnostic applications. While for therapeutic purposes, it is important to understand the ability of light to penetrate the tissue and deposit energy via optical absorption properties [1].

Invasiveness is another challenge that needs to be addressed when designing a system for deep brain research. The original form of deep brain stimulation (DBS) is the technique in which multiple electrodes are implanted in the region of interest of the brain and stimulation pulses are administered at an appropriate frequency to suppress neural activity in the subthalamic nucleus [2]. One way to improve the performance of this instrumentation is to use a single probe to penetrate the tissue as opposed to multielectrode arrays or a combination of electrodes and optical fibers which are the current techniques used in neuro-research experiments.

The recent development of an excitation and emission detection module (EEDM) that uses a single optical fiber [3] for fluorescence detection was designed to reduce the invasiveness that having a system with two probes with two paths (stimulation/detection) would cause. This system is minimally invasive as an optical fiber in the size of 200um can be used as the head of the system to travel through the brain to excite regions of interest while detecting a small signal from fluorescent molecules.

The aim of this project is to expand on the functionality and capabilities of this recent design of light delivery and detection focusing on optogentic applications. Optogentics is a neuromodulation technique that has been recently established and allows neural activity to be modulated with light. For this reason, the cells of interest are genetically modified, giving them the ability to produce proteins that are sensitive to light [4]. The introduction of these proteins into brains of live animals or cells of interest with the use of fluorescent biomarkers provides a methodical approach to track light sensitivity of neurons. This project introduces and tests an instrument to extract the location and depth of maximum light sensitivity of the fluorescent distribution following gene delivery which optimizes optical stimulation.

In this chapter, the reader will be presented with behavior of light in tissue as well as a modeling technique used for light propagation in tissue and an overview of optogenetics which has been around since the early 2000s and has become a powerful technique for neural studies across the fields of science and engineering. The chapter will conclude with the description and background of the recent detection and stimulation platform that this new imaging device is based on.

1.2 Introduction to Light-Tissue Interactions

By observing the interaction of light with media we are able to describe the optical properties of specific tissue. Figure 1.1 shows different types of interactions that are possible between light and scattering tissues such as brain, breast, and skin. These situations include absorption scattering, fluorescence, reflection, and transmission [5].

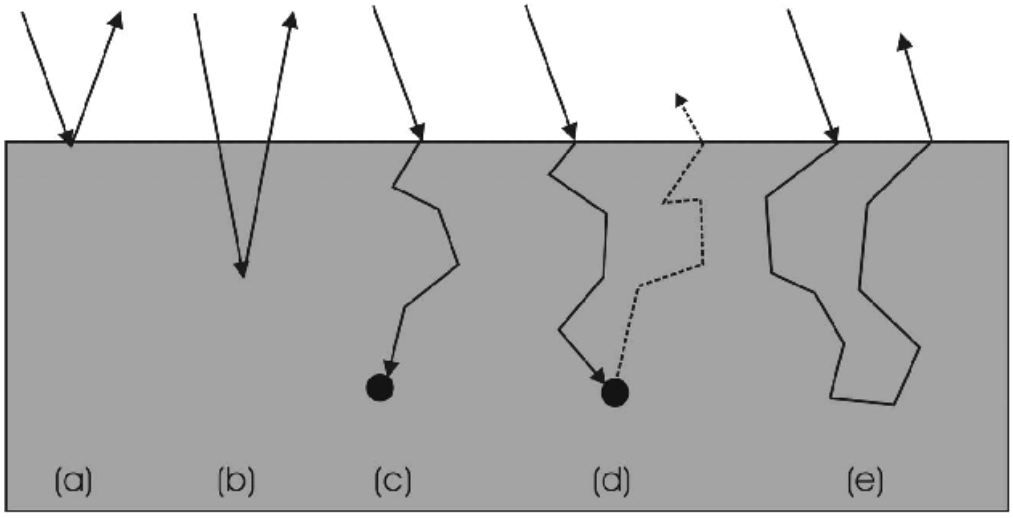

Figure 1.1 Different types of interaction of light with tissue (a) reflection (b) back scattering (c) Absorption (d) fluorescence/Raman scattering (e) diffuse Reflectance. Black dots shown are either tissue chromophore, fluorophore or a scatterer [5].

Light propagation in tissue depends on the scattering and absorptive properties of its components, and can cause a laser beam to widen or deteriorate as well as beam dispersion. Other factors that influence the propagation of light in tissue are size, shape, and concentration of tissue particles as well as polarization of the incident light in tissue [6]. One of the first phase in designing a device is to stipulate the optical properties of the tissue under study. These properties can include the absorption, scattering, anisotropy, reduced scattering, and refractive index. Figure 1.2 shows the optical properties [1]. θ represents the deflection angle and Ψ represents the azimuthal angle.

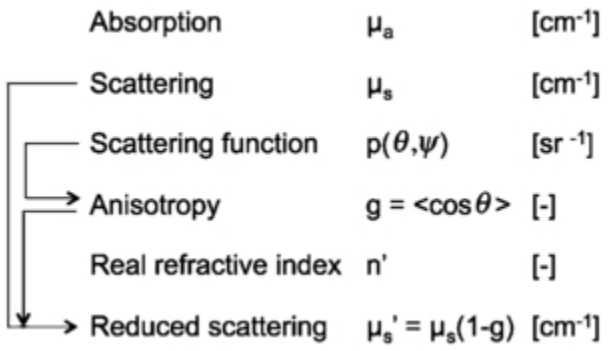

Figure 1.2 Optical properties of tissue [1].

These properties are calculated and measured through experimental methods and using optical theories, which will be covered in the following chapters.

1.2.1 Absorption Coefficient

As light waves propagate through a medium, the energy of photons can be transferred to molecules from matter. This behavior is known as absorption. This effect causes a decrease in the light intensity that is ultimately transmitted. The absorption coefficient μ_a [cm^{-1}] quantifies

whether a photon is absorbed per incremental pathlength of within a medium. A large absorption coefficient corresponds to higher attenuation of the number of photons that travel in the tissue. This means that light will more rapidly loose intensity compared to a lower absorption coefficient which occurs in media that is comparatively transparent [7]. This parameter is wavelength dependent and also depends on materials in which light travels. The absorption can be relatively large for shorter wavelengths which accounts for limitations on the penetration depth of light.

Chromophores are groups of atoms within organic molecules that are responsible for the absorption of photons and can absorb different wavelengths. The absorption coefficient of a tissue is calculated by taking into account all contributions from all of its absorbing chromophores and can be found using the extinction coefficient ε_i, concentration of chromophores C_i and the wavelength λ [1]:

$$\mu_a = \sum_i C_i \, \varepsilon_i(\lambda) \, . \tag{1}$$

There are a number of chromophores that are natural or exogenous, which contribute to the absorption coefficient equation. However, the dominant contributors considered are blood, water, and in some cases melanin and fat.

1.2.2 Scattering Coefficient

When scattering occurs, photons can drastically change their direction of motion which results in ambiguity regarding the path along which light travels in the tissue, it broadens light beams, and limits the penetration depth of light as photons are now changing directions considerably as they travel through the medium. The scattering coefficient μ_s [cm^{-1}] quantifies how frequently a

photon is scattered in the tissue. This parameter is inversely proportional to wavelength and is described in terms of unit pathlength. The scattering coefficient can be determined by [1]:

$$\mu_s = -\frac{\ln(T_C)}{L}. \quad (2)$$

T_C is the measured collimated transmission through a tissue thickness of L. These measurements are made through a thin tissue sample which is usually in the scale of the mean free path ($1/\mu_s$) or less. This could prevent issues that may arise from multiple scattering events in biological tissues. However, preparing such small samples present challenges which can cause an error in the estimation of μ_s. One of these challenges is the angle of detection. If this angle is big enough, an underestimation of μ_s potentially occurs due to the collection of photons regardless of their small angle of deflection.

For these reasons, the value of μ_s may not always give reasonable results, and in the case for multiple scattering, a more reliable value would be that of the reduced scattering coefficient $\mu'_s[cm^{-1}]$. The reduced scattering coefficient can be determined by:

$$\mu'_S = a\left(\frac{\lambda}{500(nm)}\right)^{-b}, \quad (3)$$

where the factor *a* is a scaling factor and has the value of μ'_s at a value for λ of 500nm, λ is the wavelength, and *b* is the scattering power which is the parameter that characterizes the dependence on the wavelength [1]. We can also define the reduced scattering coefficient using anisotropy factor *g* as defined by:

$$g = \langle cos\ \theta \rangle, \quad (4)$$

$$\mu'_S = \mu_S(1 - g). \quad (5)$$

The anisotropy factor g is described by the average cosine of the scattering angle. This is known as the Henyey-Greenstein phase function. The typical values for g are between 0 and 1 due to the deflection angle θ. The value of g = 0 corresponds to isotropic scattering and g = 1 is totally forward scattering [8]. Usually, the value of g in biological tissue is around 0.9.

1.2.3 Fluorescence

Fluorescence imaging allows researchers to study the functionality of tissue in different applications as well as the structural features of the tissue. Fluorescent dyes can be distinguished in small quantities without using radiations that might have a negative effect to the tissue under study. The mechanism of fluorescence transpires when the energy from a photon is absorbed by a fluorophore at its which then results in an emission of a lower energy photon with a longer wavelength compared to that of the excitation light.

The process of fluorescence starts with the absorbance of a photon by a fluorophore molecule which is excited by the energy of that photon. Then the excited electrons transition non-radiatively to the lowest energy level. Finally, the excited molecule returns to the ground energy state by releasing the extra energy in the form of an emission photon with a longer wavelength [9]. Figure 1.3 represents this mechanism using the Jablonski energy diagram [10].

Figure 1.3 Jablonski energy diagram. Straight-line arrows represent the radiative transition between energy states. The curved - line arrows represent transitions that are non-radiative. Adapted from [10].

For fluorescence imaging the idea is to use a light source of an appropriate wavelength as a way to excite the fluorescent molecules which then emit light with a longer wavelength and less energy. It is important to understand the difference between these two wavelengths for the proper design of any fluorescence imaging/detection instrumentation.

For in-vivo experiments we use fluorescence proteins, such as green fluorescence protein (GFP) which is a form of exogenous florescence probe that is normally employed to provide information about living tissues. Compared to dyes that lack specificity, Fluorescence proteins are expressed in particular cellular and subcellular compartments [11]. Figure 1.4 shows the excitation and emission spectra of GFP [12]. In this figure, we can see the difference in peak excitation to peak emission known as the Stoke shift. For GFP, the optimal excitation wavelength is 488nm while the optimal emission wavelength is 507nm. EGFP is and enhanced form of GFP with brighter fluorescence.

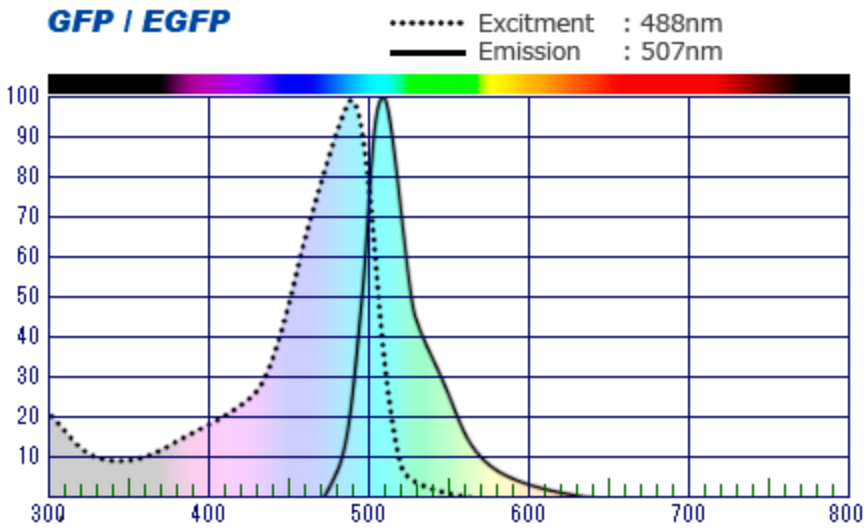

Figure 1.4 Excitation and Emission Spectra of Green Fluorescence Protein [12].

1.2.4 Light-Tissue Interaction Simulation

A vital step in the design of instrumentation for fluorescence imaging/detection is to use the understanding of optical properties in a model to simulate light propagation in biological tissue and predict the light distribution in the tissue under study. Typically, the radiative transport equation (RTE) is used to model the movement of light inside tissue [13]. RTE is formulated by [14]:

$$\frac{\partial L(\vec{r},\hat{s},t)/c}{\partial t} = -\hat{s}\cdot\nabla L(\vec{r},\hat{s},t) - (\mu_a+\mu_s)L(\vec{r},\hat{s},t) + \mu_S\int_{4\pi} L(\vec{r},\hat{s}',t)P(\hat{s}',s)d\Omega' + S(\vec{r},\hat{s},t), \qquad (6)$$

where the term $L(\vec{r},\hat{s},t)$ represents the radiance, $P(\hat{s}',s)$ is the phase function, and $S(\vec{r},\hat{s},t)$ is used to describe the light source [7][14].

In order to simplify the complexity of the RTE, assumptions are made to reduce the number of variables involved [7]. One of the assumptions leads to the isotropic radiance while another assumption concludes that the fractional change in the tissue density is much less then unity over the mean free path. This gives a much simpler approach to modeling light propagation in tissue known as the diffusion approximation, in which the diffusion coefficient is described by:

$$D = \frac{1}{(\mu_a + \mu_s(1-g))}. \tag{7}$$

However, the assumption that the radiation in the medium is almost isotropic discards this modeling technique as an option for our simulation because this model is not fitting for the single fiber scanning probe system that is being proposed, where the distance between the source and the detector can be less than $\frac{1}{\mu'_s}$. Another approach which displays higher accuracy while the diffusion approximation breaks down is the stochastic approach based on Monte Carlo (MC) [15][16].

1.2.5 Monte Carlo

In the MC method, propagation of many photons are modeled using the theory of random walks. By tracking enough of these photons an estimate of the physical properties can be made by introducing random variables as the physical quantities that we would like to quantify such as diffuse transmittance. The necessary parameters that are needed for simulations are absorption, scattering, and anisotropy coefficient or phase function. Depending on the optical properties chosen, photons can have different interactions with the tissue, such as absorption, scattering or

reflectance. MC tracks all these interactions while recording them to create an ensemble average, which can be a quite accurate approximation to the real values, of the mentioned quantities.

Figure 1.5 shows the flow chart for MC modeling of the propagation of a photon packet. The photon is first launched with an initial weight. After that, the photon is moved by a differential step size (Δs) which is randomly assigned given the absorption coefficient, scattering, and anisotropy factor. As the photon moves freely through the tissue multiple interactions can occur including transmission out of the tissue. After the completion of this step, the weight of the photon is updated. The interactions that occur are recorded. For example, if the photon is absorbed, the location of absorbance is recorded and if the photon is reflected, that event is recorded. The same goes for transmittance but not for scattering. Scattering simply changes the travel direction of the photon. In this case, a new scattering angle is assigned randomly as well as a step size. One step at a time, the photon packet travels through the tissue until one of two events happen. Either the photon is absorbed or it leaves the tissue. In either case, a new photon is launched. This process continues until the preset number of photons are launched and their paths are determined. The culmination of this process produces an accurate estimate for the absorption, reflection, and transmission.

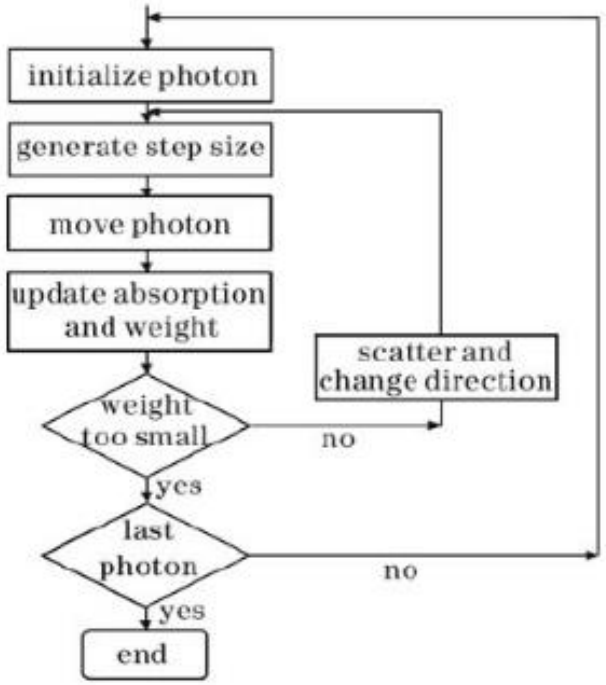

Figure 1.5 Flowchart of MC modeling of photon propagation. Once a photon packet has been initialized, Δs is determined and the photon is moved. All the interactions with the tissue are recorded and the photon weight is updated. The photon is terminated when its weight is under a threshold. A new photon is then launch into the tissue [15].

When modeling the distribution of fluorescence, a new parameter needs to be accounted for. The quantum yield of a photon determines how effectively that photon packet interacts with fluorophore molecules to create a new photon of different wavelength. The flowchart for the fluorescence MC model is presented in Figure 1.6. A photon with an excitation wavelength λ_{exc} is launched in the similar way as a regular MC simulation. This wavelength determines the optical properties used for this tissue. The quantum yield gives a probability for the excitation photon to be absorbed thereby creating a fluorescence photon of emission wavelength λ_{emm} after a short delay. The rest of the simulation runs as a typical MC simulation using updated values for the absorption, scattering, and phase function for λ_{emm}.

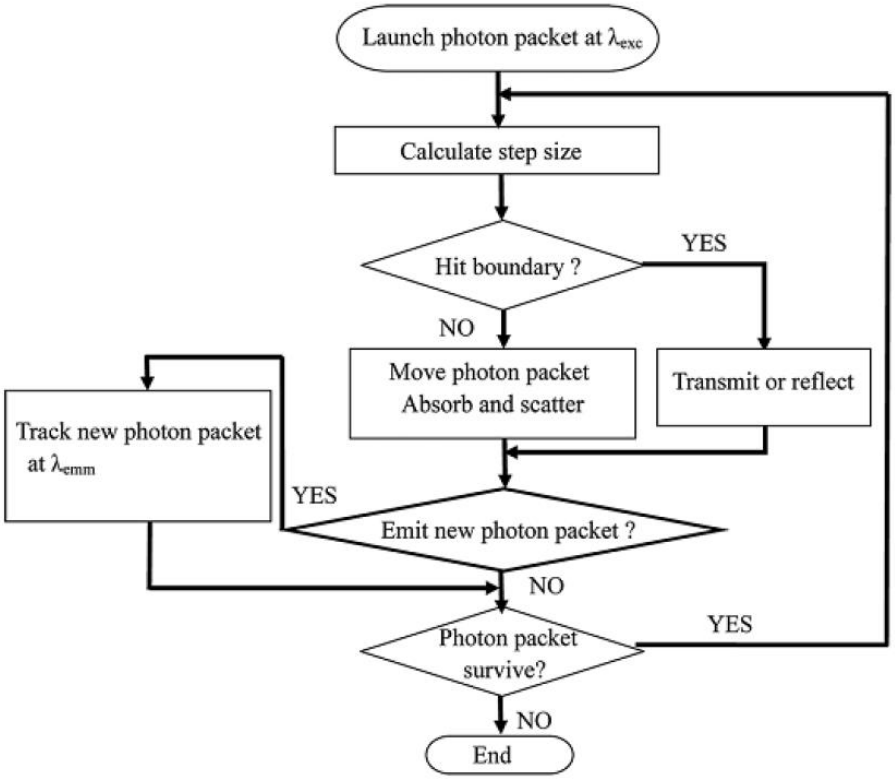

Figure 1.6 Flow chart depicting the model of MC with fluorescence. A photon is first launched using the excitation wavelength. Once the photon is absorbed, the fluorescence photon is created and the fluorescent light is simulated with updated optical properties using the new wavelength of fluorescence emission [16].

While MC can be an effective and reasonably accurate approach to model light propagation in turbid media, it can be quite costly computationally due to the statistical nature of the method. The larger the quantity of photons used, the more accurate the approximations are. However, there are instances when a large number of photons is not necessary. For example, if there is an interest in learning the total reflectance of the tissue, 3,000 photons would be typically needed to obtain a good approximation. However, for applications where spatial distributions need to be mapped in a more complex problem, over 100,000 photons may be required. The number of photons used will depends on the study[17].

1.3 Neurons and Optogenetics

There are many neuropsychiatric illnesses that could profit from a better understanding of the functionality and connections of particular cell types within networks of neurons in the brain [18]. Optogenetics provides bi-directional control of neurons with milli-second temporal resolution by introducing light-sensitive proteins, originally adapted from algae and bacteria, into neurons [19]. In this section, a brief overview of the structure and functionality of a typical neuron is provided before discussing the neuromodulation technique of optogenetics.

1.3.1 Neuron

Figure 1.7 shows the physiology of the neuron [20]. Neurons are electrically excitable cells in the nervous system that are responsible for processing and transmitting information. Inside and outside neurons there are many positively and negatively charged ions. The membrane potential is the difference in the net charge of the inside versus outside. In the cell membrane, there are proteins that function as gates that allow ions to travel in and out of the cell called ion channels and ion pumps. Some of these proteins are voltage dependent and function at or over specific cell membrane threshold voltages. The threshold voltages are reached when there is an influx of positive ions into the cell. Passing the threshold triggers a process which leads to the generation of an electric spike by the cell which is known as action potential. This pulse propagates along the neuron until it reaches the synaptic sites. When the action potential arrives at the synapses, the cell releases chemicals which stimulated the post-synaptic neurons and the process continues. Voltage gated ion channels are involved in signal transferring within the cell and releasing neurotransmitters at the axon terminals.

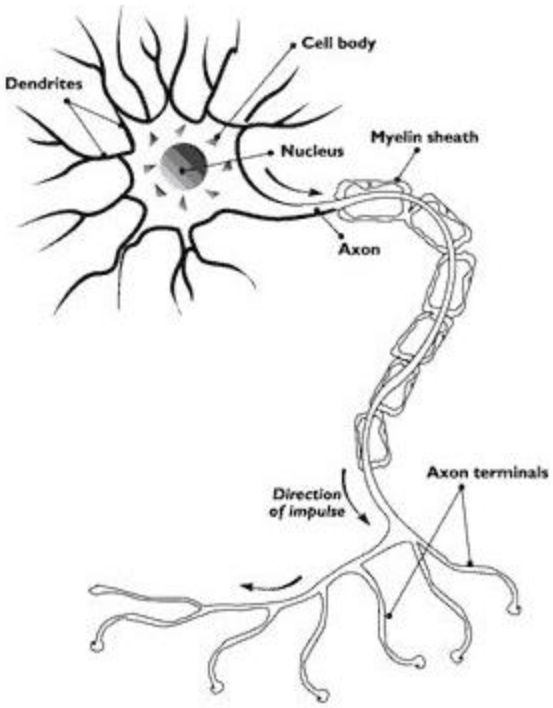

Figure 1.7 Physiology of a neuron. A signal is detected by dendrites, is processed through the soma (cell body) and axon as it travels to the axon terminals [20].

Dendrites behave like antennas, receiving signals from other neurons. The soma (cell body) contains many organelles and the nucleus. The function of the axon is focused on the transferring of information away from the cell body. The action potential travels along the axon as a voltage pulse until it reaches the synapse sites at the axon terminals. It is at these terminals that the electric potential undergoes a change into a chemical signal that is transported by neurotransmitters to the post-synaptic neuron. In the post-synaptic neuron the chemical signal transforms back to an electrical signal.

The resting potential of a neuron is approximately -65mV which is the condition in which the ion concentration inside compared to outside the cell is at equilibrium. In this particular state, the neuron is capable of receiving input stimulation from other neurons. The main ion

concentrations that contribute to create this balance are K^+, Na^+, Ca^{2+}, and Cl^-. If a large number of positive charged ions are allowed to enter the neuron through ion channels, then the cell experiences depolarization. This is when membrane's electric potential drifts in the direction of a positive voltage. However, if a cell allows negatively charged ions in, the cell gets hyperpolarized. This is the state in which the voltage undergoes a dip towards a more negative electric potential which prevents generating any action potentials.

1.3.2 Optogenetics

In optogentics, light can be used as a way to communicate with cells through the use of light sensitive proteins called opsins. These opsins, originally taken from algae or bacteria are produced in the neuron through genetic manipulation of the cells [18]. The role of these light gated opsins is to work as selective ion channels. Light gated channels in optogentics will allow bidirectional control of membrane potentials [21]. Figure 1.8 gives a visual representation of two microbial opsins. One example of these opsins is Channelrhodopsin-2 (ChR2), which is a light-gated ion channel with maximum light sensitivity to the wavelength ~ 445nm. When ChR2 is stimulated by light of this wavelength, Na+ and Ca^{2+} are allowed into the cell which induces depolarization leading to an action potential. Another example is halorhodopsin (NpHR) which behaves as a Cl^- pump driven by light. The proper excitation wavelength for NpHR is ~570nm. When exposed to this wavelength Cl^- anions are pumped into the cell which results in hyperpolarization thus hindering the neuron from firing.

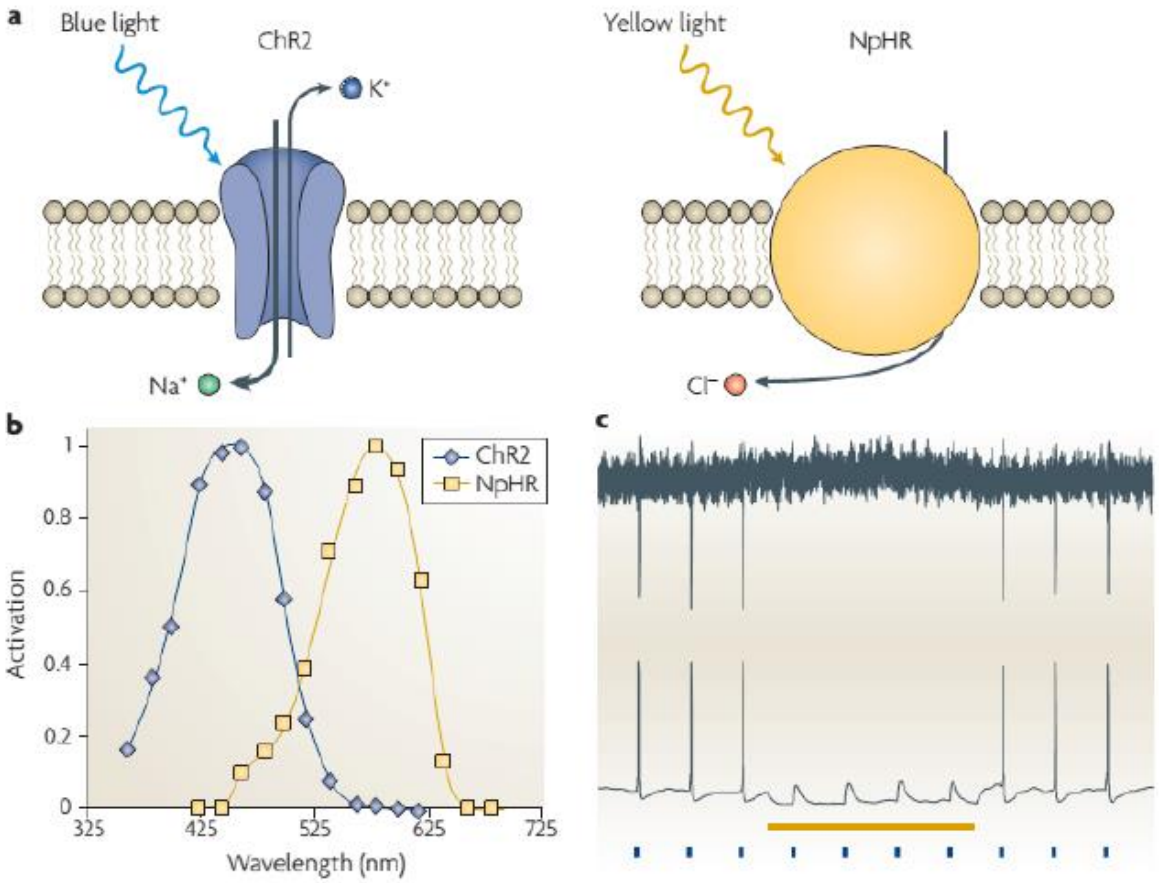

Figure 1.8 (a) Left depicts channelrhodopsin-2 (ChR2) and Right depicts halorhodopsin (NpHR) . ChR2 allows Na^+ into the cell when stimulated with blue light. NpHR pumps Cl^- into the cell when stimulated by yellow light. (b) Spectral activation of ChR2 and NpHR. The difference in spectrum allows activation and inhibition in the same cell population. (c) demonstration of both stimulation using ChR2 and inhibition using NpHR [18].

Verification of gene expression is necessary for successful experiments with optogentics. To confirm the proper expression of light sensitive proteins, fluorescent proteins, such as GFP and YFP, are employed as biomarkers. The genetic code for opsins are tagged with fluorescent proteins before being delivered to the cells. In the case of GFP, if the cell is illuminated with blue light after gene delivery and there is an emission of green light, the expression of light sensitive proteins is verified [22]. For YFP, confirmation of protein expression occurs when stimulation of the genetically modified cell with green light results in emission of yellow light.

Currently, the typical method for gene expression verification is to euthanize the animal following optogentic experiments. The brain is then extracted and sliced and the fluorescence distributions are imaged using fluorescence microscopy.

The use of fluorescence proteins has proven to be useful in optogentics because it can also provide a mechanism for observing neural activity. For example, having a fluorescent signal as an output for a change ion concentrations in the neuron (e.g., Ca^{2+} imaging) or changes in potentials (e.g., voltage sensitive dye imaging) [23].

The main benefit of using light for neuromodulation stems from the cell specific targeting capabilities in optogenetics. Figure 1.9 shows different approaches for modulation of neural activity [24]. There have been improvements in the classical methods for the study of neural activity but some restrictions remain that limit the function of those methods when compared with optogentics. Electrical and physical approaches have undesired effects on the area surrounding the probe. Pharmacological and genetic methods lack the temporal resolution that is sometimes necessary for neural studies. Using light provides the best approach but one major challenge is the delivery of excitation light and fluorescence detection in areas of interest due to absorption and scattering of the tissue.

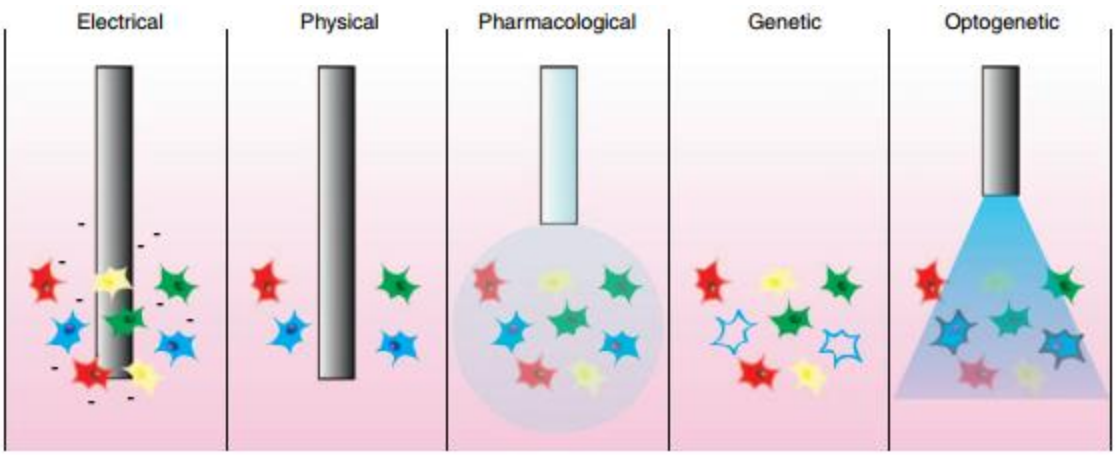

Figure 1.9 Using electrical stimulation can benefit from high temporal precision but affects all the tissue surrounding the electrode. Physical probes can reduce cell activity by cooling them, but also affect the area surrounding the electrode. Injection of a drug targets a specific cell-types, but chemicals stay in the system for longer periods of time, reducing temporal precision. Genetically modifying cells is irreversible and has reduced temporal precision similar to the pharmacological approach. Optogenetics benefits from targeting specific cell types with high temporal resolution [24].

The typical approach is to use an optical fiber that is implanted in the brain using a cannula. Since the fiber is fixed and the optical properties of the tissue affect light distributions, light delivery and detection of fluorescence are constrained to a small area near the fiber tip. By introducing motion to the fiber, we can optimize light delivery and detection. This is usually a preferred approach compared to using multiple waveguides which can be more invasive and complex due to the geometry of the set up.

The next section will cover a recently developed single optical fiber EEDM to excite fluorophore molecules at different depths in the brain and guide a sample of the emission signal back to the detectors through the same fiber.

1.4 Excitation and Emission Detection Module (EEDM)

A diagram of the EEDM [3] used in this project is shown in Figure 1.10. Designed for neuroscience and optogentic experiments, this system uses a single optical fiber for light delivery and detection of faint fluorescence signals back to a light detector. This system employs two lasers to stimulate at the wavelength of 473nm(blue) and 593.5nm(yellow) for excitation of ChR2 expressed cells and NpHR expressed cells, respectively [18][19]. However, for this project, we only use the blue laser as it is close to the excitation peak of GFP. A highly sensitive photodetector is used to detect the fluorescent signal. The detector is a Hamamatsu avalanche photodiode (APD) C4777-01. The system also includes a second detector that is used to dynamically monitor the intensity of the light that is being delivered. This allows the elimination of input light fluctuations, imperfections of optical filters, and back reflection of the excitation light. A calibration process, compensates for any self-luminesce of the optical fiber and imperfections in the emission filter.

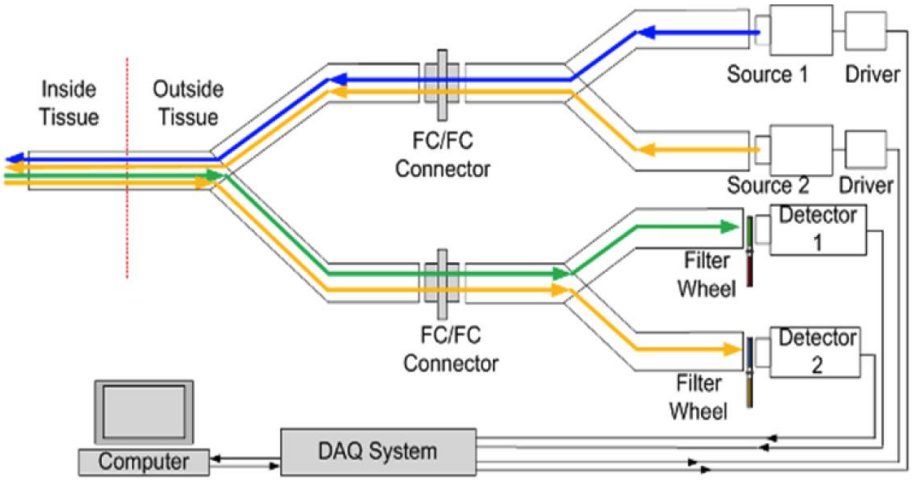

Figure 1.10 System diagram of the EEDM [3].

The EEDM uses a data acquisition device from National Instruments (NI USB-6952) which connects to a computer via a USB port. A picture of the EEDM is shown in Figure 1.11. All the electronics and optical components are enclosed within an optical absorber material and grounded copper cage to reduce effects from ambient light and electromagnetic interference. The whole setup is placed on a mobile cart to facilitate transportation. There is one opening on the enclosure for the USB and another opening for the connection of the optical fiber.

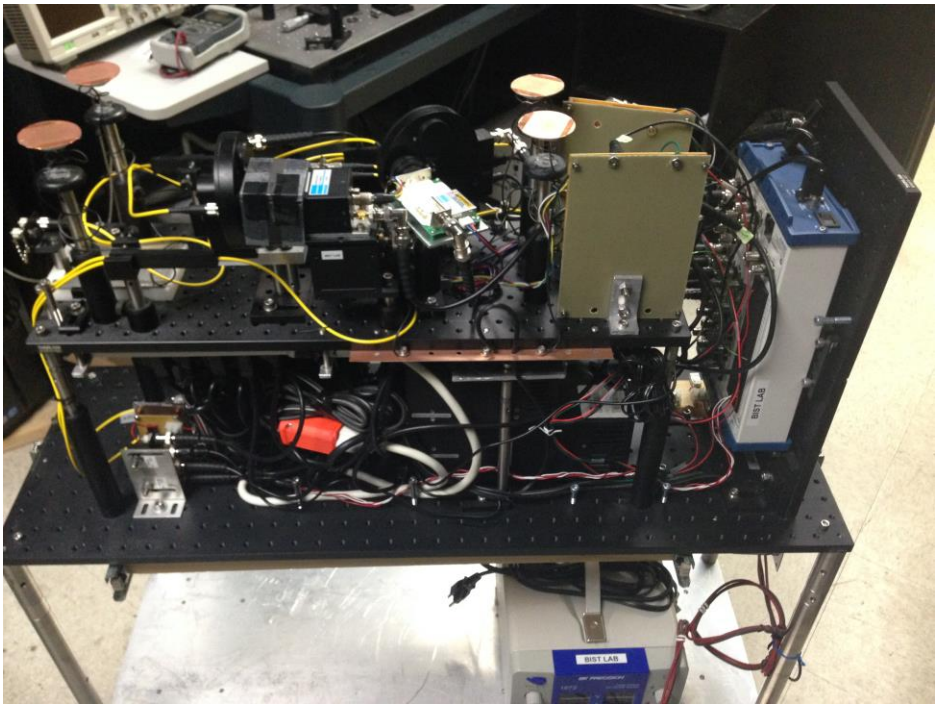

Figure 1.11 Picture of the EEDM with its enclosure off to display the inside components. Copper plates are used to reduce electromagnetic interference effects. DC power supply is the only component outside the module.

This module also provides an optimized S/N through the use of optimal filter and time-lens mechanism. It is proven that the noise in the system is white Gaussian and therefore the matched filter to maximize S/N is the autocorrelation operator [3]. This is implemented in the system by taking the autocorrelation of the photodetector output. This is done by modulating the excitation

light with a chirp pule which is a pulse where frequency is linearly swept and then compressed by passing it through a time-lens which in this case is the correlator filter. Figure 1.12 shows this effect.

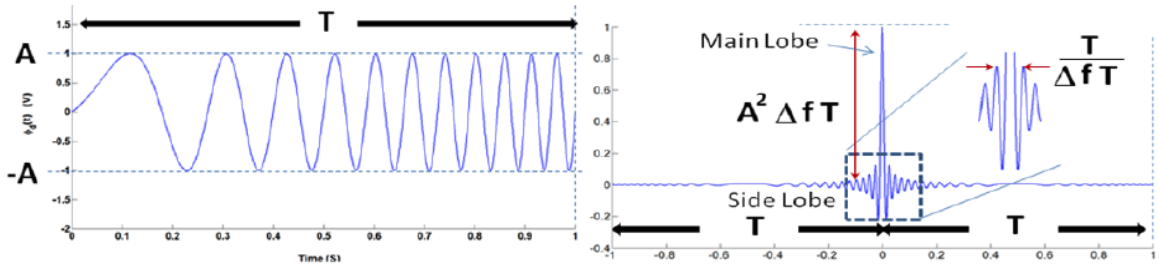

Figure 1.12 (Left)Example of a chirp pulse with amplitude from -1 to 1 and frequency linearly swept over period T. (Right) Chirp pulse is passed through the time lens which compresses the signal maximizing the power at one point [3].

The temporal resolution was also improved by overlapping the pulses and using a non-linear frequency modulated pulse called the Taylor pulse [25]. This has some effect on the shape of the chirp pulse because the frequency will no longer be linearly swept. This slightly sacrifices gain to achieve a much better temporal resolution.

While this device can use a single optical fiber to detect fluorescence signals as the fiber travels vertically through the brain tissue, it lacks the ability to capture fluorescence from different directions within the same depth. The purpose of the project is to introduce a mechanism that adds another dimension to the functionality of this module by rotating a side-firing optical fiber and sequentially moving it down into the tissue while stimulating and detecting fluorescence signals at different directions. This creates a scanning mechanism that helps in finding the area of maximum light sensitivity and the overall distribution of fluorescence. The next chapter will cover the design of the system.

Chapter 2. System Design

2.1 Introduction

In this chapter, I will discuss the design of the system. The hardware was designed with ease of transport in mind as well as how simple it is for the user to put the device together and run experiments. The availability of the components was also considered and most of the components were purchased from the Thorlabs website with the exception of two aluminum plates that were machined and a side-firing optical fiber that was customized for this particular system. The software gives the user options for a variety of parameters to adjust for a different resolution, time of scan, and areas of interest to be scanned.

2.2 Hardware

The proposed system is shown in Figure 2.1 and includes a side-firing fiber, rotation arm (rotary joint, lens tube, and fiber chuck), two servo motor actuators with their corresponding servo motor controllers, structural components needed to hold the system together, laptop computer, and the EEDM discussed in the previous chapter. The following sections will provide an overview of the hardware used in this design.

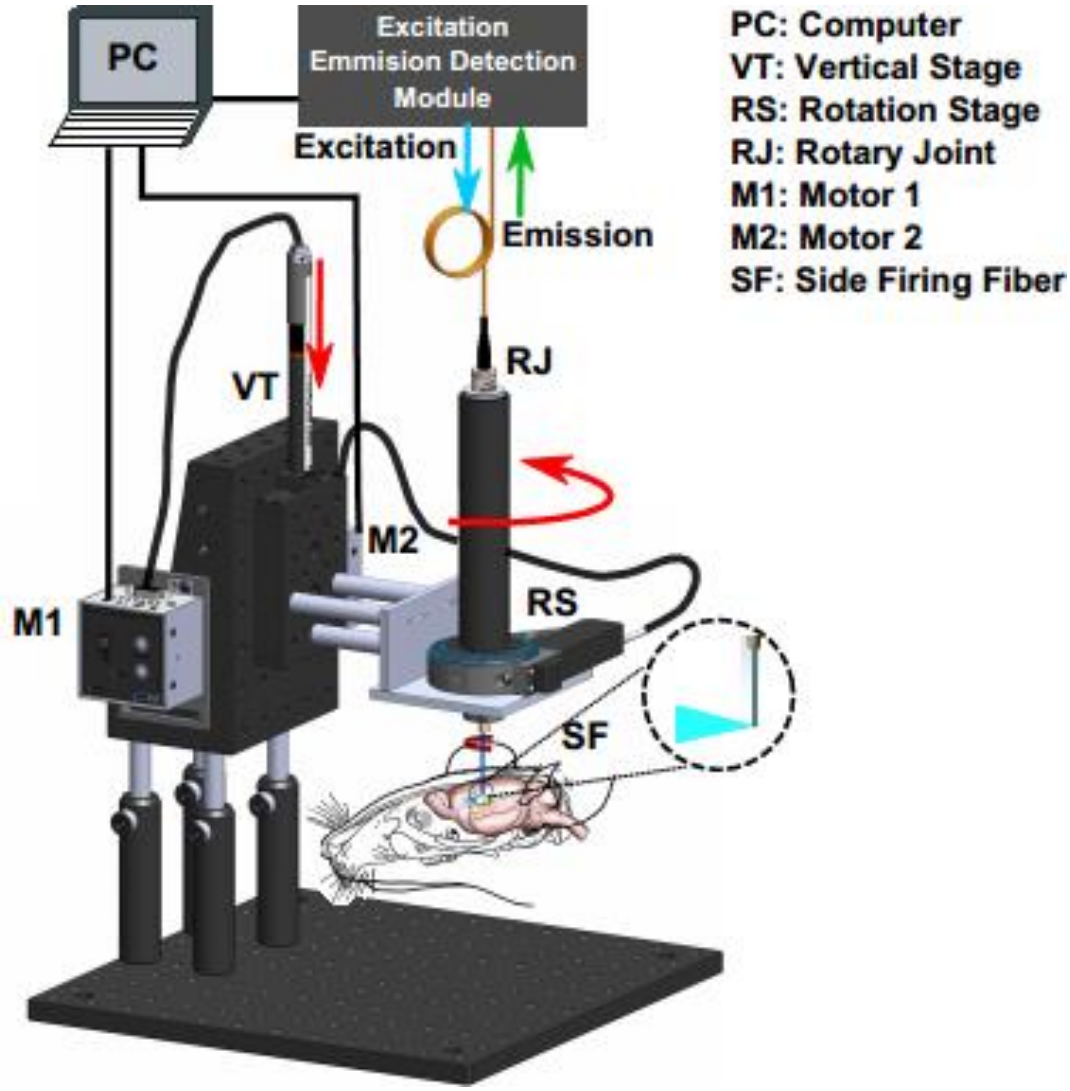

Figure 2.1 Diagram of the System Hardware. Motor controllers M1 and M2 drive the translation stages VT and RS to move the optical fiber vertically and rotate it while the EEDM delivers excitation light and detects fluorescence through the side-firing fiber SF. The rotary joint (RJ) allows rotation of the optical fiber without any twisting or damage to the fiber.

2.2.1 Side-Firing Fiber

The EEDM allows us to use a single optical fiber with the system, thereby making it less invasive. Side firing fibers have been used in applications such as dentistry and ablation [26][27]. Figure 2.2 Shows how a side-firing fiber functions. Following ray optics approximations, which can be used since the wavelength is much smaller than the core and

cladding of the fiber, we can analyze the light path as it radiates out of the fiber. Light experiences total internal reflection as it hits the tip of the fiber. The desired effect is to obtain $\Psi_{mid} = 90°$. This is accomplished by increasing the angle of the fiber tip Φ. The fiber tip angle has a limit which prevents Ψ_{mid} to reach 90°. It is shown in [3] that for a fiber with numerical aperture (NA) = 0.22 the optimal delivery angle is 38° and for a fiber with NA=0.37, it is 32°.

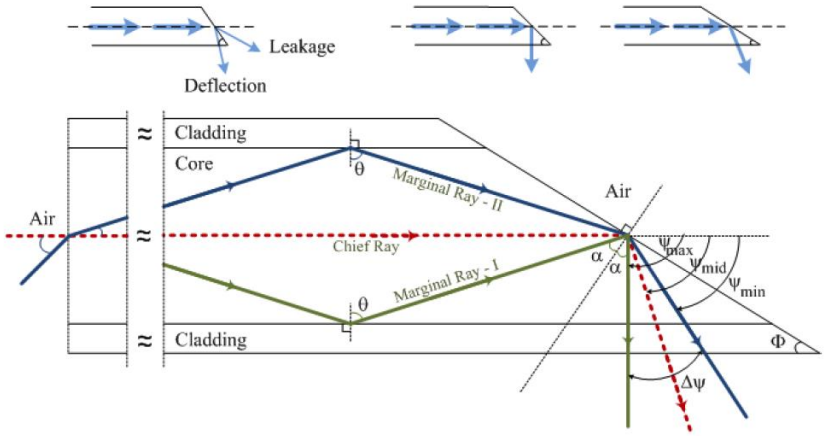

Figure 2.2 Side-firing fiber analysis using ray optics approximations [3].

For the side-firing optical fiber in our system we used a custom-made high OH silica core optical fiber (Polymicro Technologies) with the delivery tip angle of 40° and core diameter of 200µm. To measure the divergence angle of the radiation cone, I used a 1.3 Megapixel CMOS camera (Thorlabs DCC1645C) to take a picture of the fibers radiation profile. Figure 2.3 shows the profile of the side-firing optical fiber. I was then able to calculate the angle of the acceptance cone by first fitting a circle to the image of the distribution of light using the FWHM. Using the distance from the fiber to the detector plane of the camera which is 1.575mm and the radius of the FWHM circle the angle can be calculated. This calculation is done by using the number of pixels in the radius of the circle times the size of each pixel which is 3.6µm.

This measurement is used to calculate the NA of the fiber as:

$$\theta = tan^{-1}\left(\frac{3.6 * 10^{-3} * 160}{1.575}\right) = 20° \quad (8)$$

$$NA = \sin(20°) = 0.34 \quad . \quad (9)$$

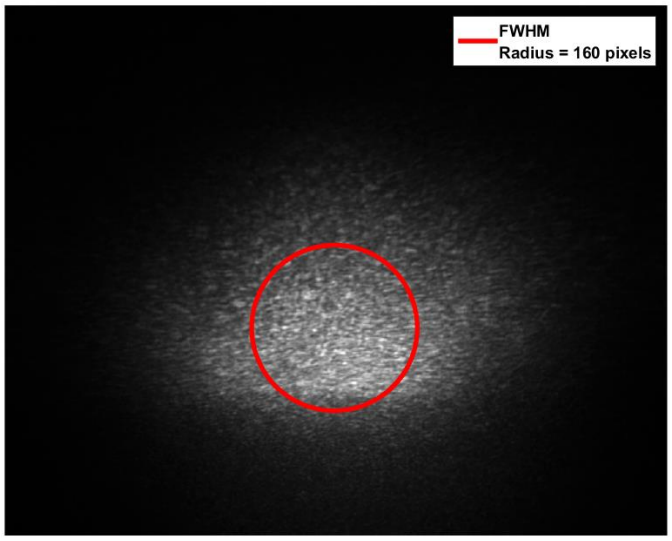

Figure 2.3 Radiation profile of the fiber. Red circle represents the FWHM threshold. The radius of this circle is used to calculate acceptance angle of the optical fiber.

Another important characteristic of the fiber is the firing angle. In order to measure this, I used the same method from Figure 2.3. We know that we placed the fiber at the center of the detector, however, by looking at the image the cone is not at the center. Measuring the number of pixel from the center of the cone to the center of the image (127 pixels) and then multiplying this number by 3.6μm gives the vertical displacement of the beam. Since we know the distance from the fiber tip to the detector plane, a simple calculation gives:

$$Firing\ Angle = 90 - tan^{-1}\left(\frac{127 * 3.6 * 10^{-3}}{1.575}\right) = 73.81° \quad . \tag{10}$$

2.2.2 Rotation Arm

The rotation arm of the system is comprised of two 2" lens tubes (SM1L20), fiber optic rotary joint (RJPSF2), fiber chuck (HFC005), and fiber chuck rotation mount (HFR001).

Rotary Joint

The rotary joint in the rotation arm allows the optical fiber to freely rotate without causing any damage to the optical fiber that would otherwise occur from twisting the fiber while rotating. One end is connected to the light source located in the EEDM while the other end is connected to the side firing fiber by using an FC/PC to FC/PC mating sleeve.

An important consideration of the rotary joint, is the coupling during rotation. To measure these fluctuations, the rotary joint was connected to a 470nm fiber coupled LED (M47051 Thorlabs) and the other side to an optical fiber delivering light to a power sensor (S130C). The rotary joint was then rotated and the power sensor output reading was observed. We noticed a distinctive characteristic in the behavior of the output fluctuations. These small differences can affect results when measuring faint fluorescence signals or visualizing data and need to be compensated. To understand this behavior, the distortion was measured 6 times, averaged, and the result is displayed in Figure 2.4. From the image on the left we can see that there is a tendency for the rotary joint to increase the detection intensity at the angle of ~150°. In order to compensate for this distortion, a distortion coefficient was created by taking the complement of the original distortion. This accounts for the highest intensity in the fluctuation to have the least

value in the distortion coefficient and vice versa. The image on the right shows the distortion coefficient used to compensate the inherent behavior of the rotary joint.

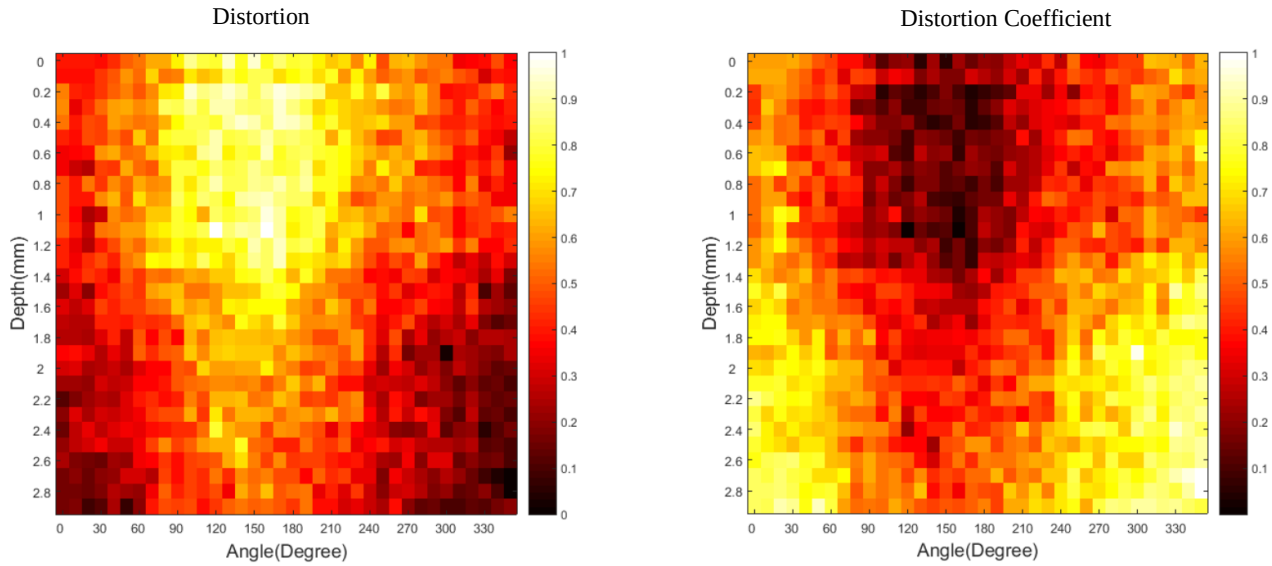

Figure 2.4 Fluctuations caused by the rotary joint(left) introduces a spike in intensity readings at 150 degrees. To compensate this effect, the complement was created as a distortion coefficient that cancels the effects(Right).

Fiber Chuck

An important element in the structure of the rotation arm is the fiber chuck that is used to hold the side firing fiber. The fiber chuck accepts optical fibers with diameters of 200um which is the diameter of our optical fiber. The fiber is fed through the length of the chuck but it needs to be done with caution to avoid causing any damage to the tip of the side-firing fiber. A collet mechanism holds the fiber in place. The chuck is mounted on a rotation mount that is designed specifically for the chuck. The mount is threaded and connected to the underside of the rotation stage. When fixing the chuck to the rotation mount, care needs to be taken to tighten the three

nylon-tipped set screws that secures the fiber chuck. The set screws need to be adjusted sequentially, one revolution at a time until chuck is firmly secured. If this is not done properly, the fiber will not rotate along its axis but will have an elliptical trajectory as shown in Figure 2.5.

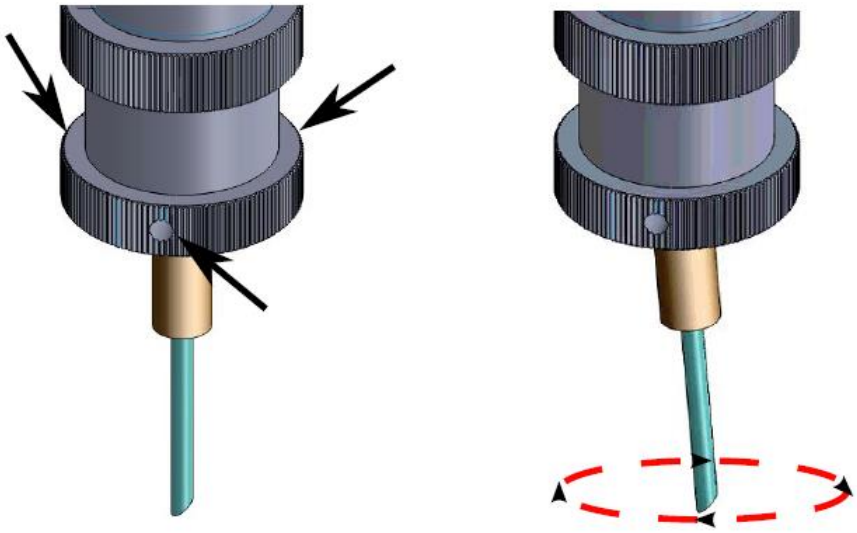

Figure 2.5 (Left) Arrows point to the position of the set screws that need to be adjusted to keep the chuck aligned along the vertical axis. (Right) Undesired trajectory of optical fiber resulting from improper set screw adjustment.

2.2.3 Movement

Vertical Translation

For vertical translation of the rotation arm, a vertical stage servo motor actuator is used. To allow for flexibility in travel distance, we used the PT1-Z8 actuator from Thorlabs. An important consideration with this component is the vertical weight capacity. For this device, the weight capacity is 8.8lbs which is more than the 2.61lbs of the combined weight from the rotating arm, rotation stage, aluminum plates, and posts used. This stage provides a dynamic range for the travel distance of 25mm. This can account for any adjustment that needs to be

made in height as well as account for dimension of the whole rat brain which is approximately about 9mm from superior to inferior.

Rotation

The rotational stage (PRM1Z8 Thorlabs) was used to rotate the fiber 360 degrees around its axis with a speed of 25deg/sec. This stage provides 0.1% on axis accuracy and 3.3lbs of on axis load capacity which is enough for our application. To attach the rotation stage, two rectangular aluminum plates needed to be machined to maintain the probe perpendicular to the horizontal plane. Each servo motor actuator is connected to its corresponding T-cube motor controller (TDC001 Thorlabs) via 15-way D-type connector. The motor controllers are connected to the computer via USB port.

2.2.4 Structural Components

For the system to be physically stable, we needed to use a base which would have a large enough area to hold up the weight of the arm without shaking or moving. A 12"by 12"optical breadboard from Thorlabs an acceptable option for the base and four optical posts and post holders for small height adjustments of the assembly. The system uses a large right-angle bracket to form the body that holds all components together.

2.3 Software

The motors are controlled via USB connections to a laptop computer and LabVIEW (National Instruments Inc.) was used to control the motion of the actuators as well as the EEDM. Figure 2.6 shows the control panel used to control the system. Multiple options were considered when designing the user interface. Options were included that would allow the user to adjust different settings to the position of the optical fiber. The"Home"button allows the user to define a new

starting point for the scanning process. When the scanning process is completed, the actuators can be programmed to return the optical fiber to its starting position or it can stop at its current position to give the user the option to explore further into the tissue.

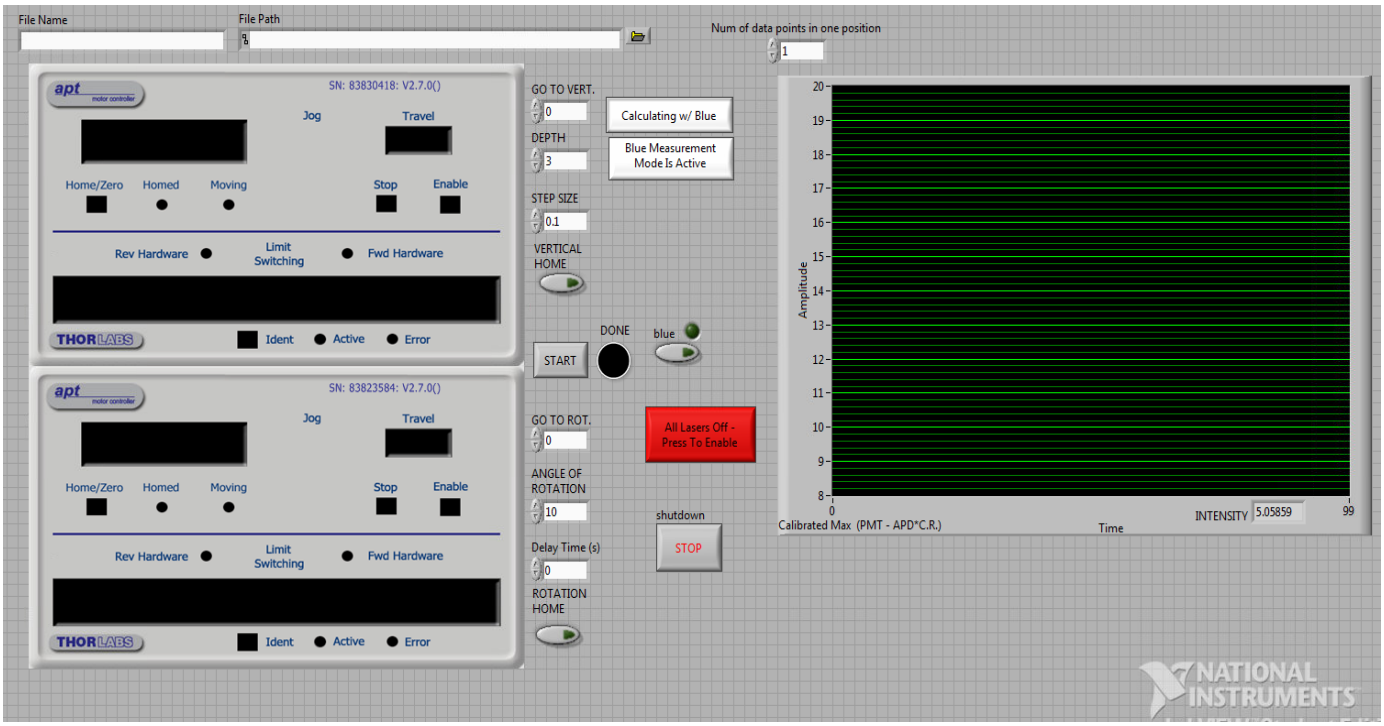

Figure 2.6 Control Panel of the system. Options are provided for the vertical motion control and rotation control. User has the flexibility to choose starting depth and scanning window size, resolution in terms of scanning angle and vertical translation step size, and number of the data points collected in each site. On the right is a continuous measurement of the intensity detected.

Chapter 3. Simulation and Performance Evaluation

3.1 Introduction

A vital step in the development of this fluorescence probe is to produce computer models which help to better understand the function of each design parameter. As mentioned in chapter 1, for simulating light and tissue interaction, MC method was used. To verify simulation results, we compared them with phantom results that are specifically designed for this purpose. In this chapter, the simulation strategy is explained and results from these simulations are presented. Phantom creation and the results from these phantom experiments are discussed.

3.2 MC Configuration

Before the simulation process was started, I calculated optical properties of the brain. To simulate optical properties of the tissue, μ'_s was modeled by:

$$\mu'_s = a \left(\frac{\lambda}{500(nm)}\right)^{-b},$$

where λ is the wavelength of the emission from a fluorescence source and **a** is a scaling factor which is the reduced scattering coefficient at λ=500nm. The **b** value is the scattering power. Values for **a** and **b** were taken from [28].

The calculation gives μ'_s:

$$\mu'_S = 23.2\ \text{cm}^{-1}$$

The μ_a was calculated by:

$$\mu_a = BS\,\mu_{HbO2} + B(1-S)\,\mu_{Hb} + W\mu_{water}\ .$$

B is the average blood volume fraction, S is the hemoglobin oxygen saturation, and W is the water content. The values for B, S, and W, were given in [28]. The absorption for hemoglobin and water was taken from the Oregon Medical Laser Center website (http://omlc.org). This gives:

μ_a = 3. 36 cm^{-1}

For g we used a typical value for the brain tissue which is 0.9.

Inputting these values into the MC simulation software [29] we can simulate the fluorescence distribution from a 250um diameter fluorescent particle. The particle is positioned 0.5mm away from the fiber with an emission wavelength of 510nm. As mentioned in chapter 1, a larger number of photons is necessary in simulations that require mapping spatial distributions. For our simulations, we used $5x10^6$ photons.

3.3 Simulation Results

In Figure 3.1 we can see the results from the simulations that account for a change in FWHM to a 250μm fluorescent microsphere with respect to the absorption coefficient. The plot on the left shows the FWHM behavior in the vertical direction of the particle with the change in absorption while μ'_s and g remain constant. There is a decrease in FWHM as the absorption increases. This accounts for more photons being absorbed before reaching the detector. The plot on the right shows the behavior of the FWHM for the radial scan in degrees. Likewise, the FWHM of the particle as absorption increases.

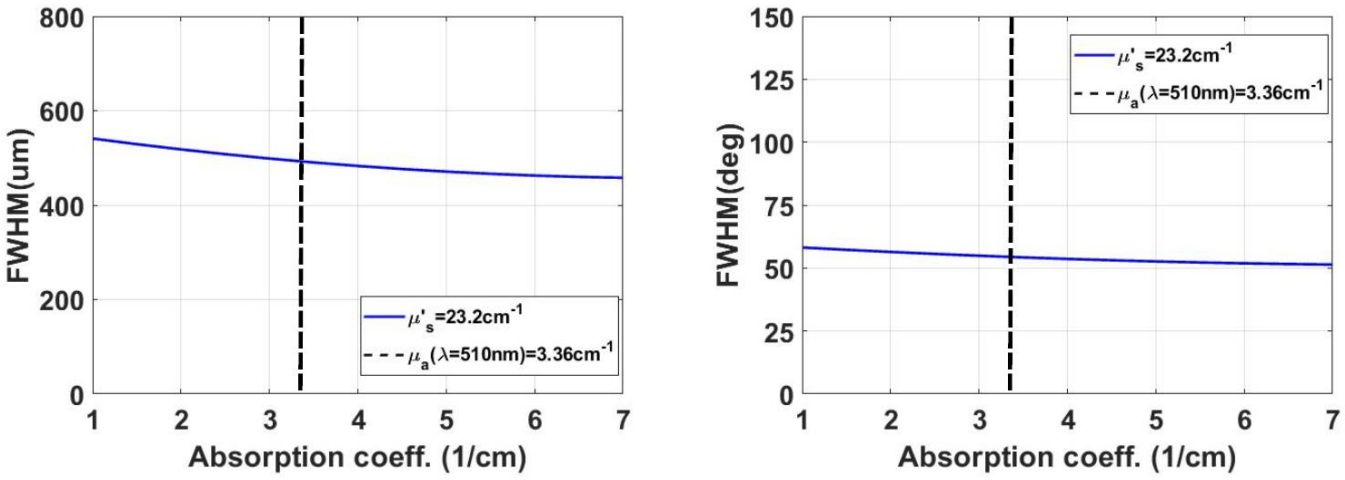

Figure 3.1 Relationship between FWHM in the vertical translation and absorption(Left). Relationship between FWHM in the radial angle and the absorption(Right). There is an exponential decay in both directions, vertical and radial, as absorption increases. Photons have a larger probability of getting absorbed as they travel farther from the source.

Changes in scattering were also simulated. Figure 3.2 shows the relationships of the FWHM with respect to vertical and radial directions, and the change in scattering while absorption remains constant at the calculated value for the brain tissue. The left plot shows the behavior of the FWHM vertically while μ'_s varies from 10 to 60 cm^{-1}. The right panel represents the FWHM behavior along the radial axis. In both cases, scattering increases the distribution of fluorescence. Scattering introduces randomness to the path that photons travel before they are collected by the detector which means that the higher the value of μ'_s, the higher the probability that the photon will change direction of travel. For this reason, see an increase in the FWHM as the scattering coefficient increases.

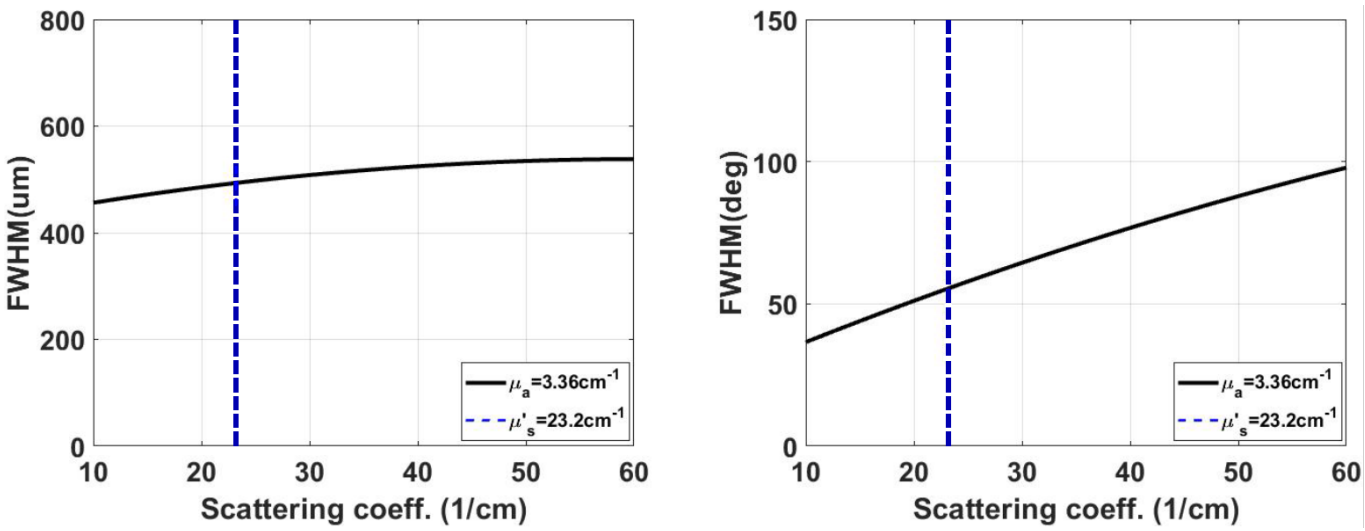

Figure 3.2 Behavior of FWHM as scattering is varied while μ_a was held constant at its calculated value of 3.36cm^{-1}. In both plots, a semi-logarithmic increase is seen. However, radially the FWHM displays an almost linear relationship to scattering.

Another way to visualize these results is to compare multiple simulations. Figure 3.3 shows four different simulation results. From this figure, we can better understand the effects of the absorption on fluorescence distribution and intensity from one value to the next. In the left plots μ_a = 1, 3, 5, and 7 cm^{-1}. The fluorescence distribution from the microspheres simulated diminishes with the increasing absorption. Absorption influences both the intensity of the fluorescence and the FWHM. Similarly, plots on the right are normalized to the highest intensity which is for the value of μ_a = 1. As μ_a increases, the distribution of fluorescence becomes smaller and intensity decreases. A change in μ_a from 1 to 7 cm^{-1} can account for a reduced intensity of about 55%.

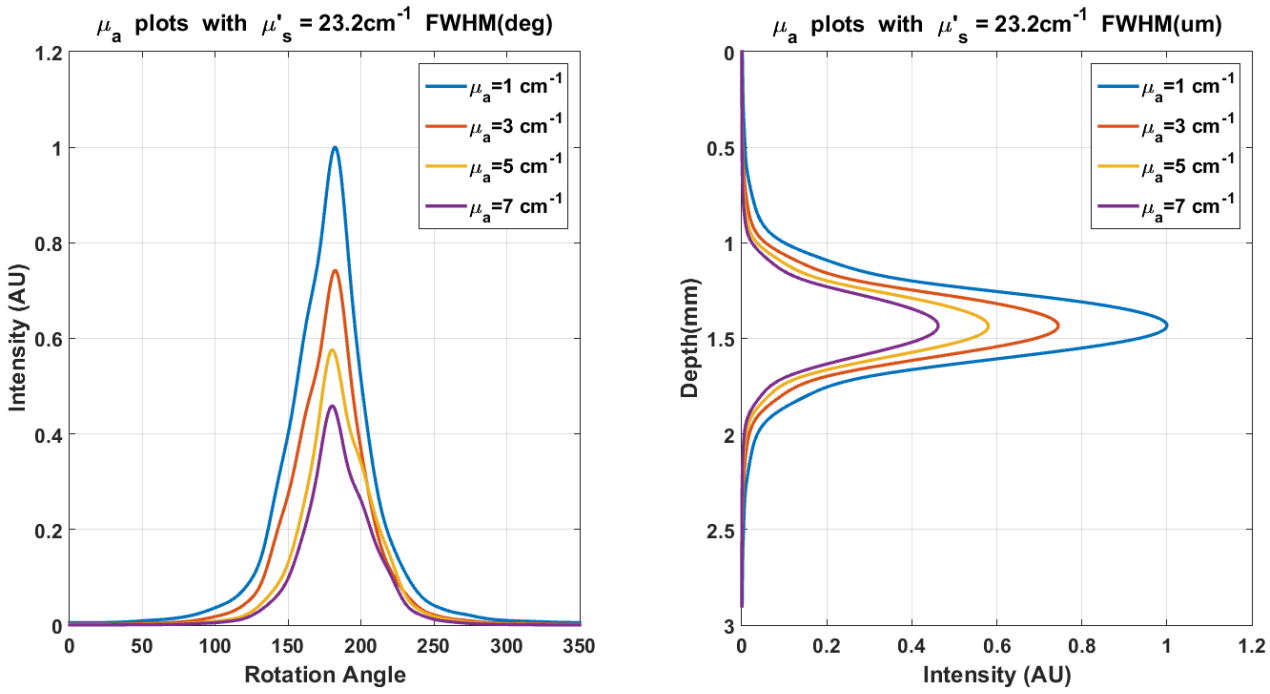

Figure 3.3 Comparison of intensity from microsphere simulations. Radial(left) and vertical(right) fluorescence distribution display similar behavior as the absorption increases. It can be seen clearly that the absorption affects the intensity of light as well as the size of the light distributions. Simulations were done for $\mu'_s = 23.2\ cm^{-1}$.

Considering the change in scattering, we can also observe its effects on the simulated fluorescence. From Figure 3.4, we can see that as scattering increases, the distribution that was once uniform is now a random shaped distribution. This also influences the point of highest intensity as it slightly shifts. The intensity reduces because the number of photons that are distributed in a small area is now spread out through a larger area. The plots on the right present fluorescent distributions along the vertical direction. In this case, we don't observe the same effects from scattering as we saw in the radial direction. This is due to the resolution of the simulations. In this simulation, the resolution for the vertical direction is too large (=.25mm) which does not show the effects of scattering.

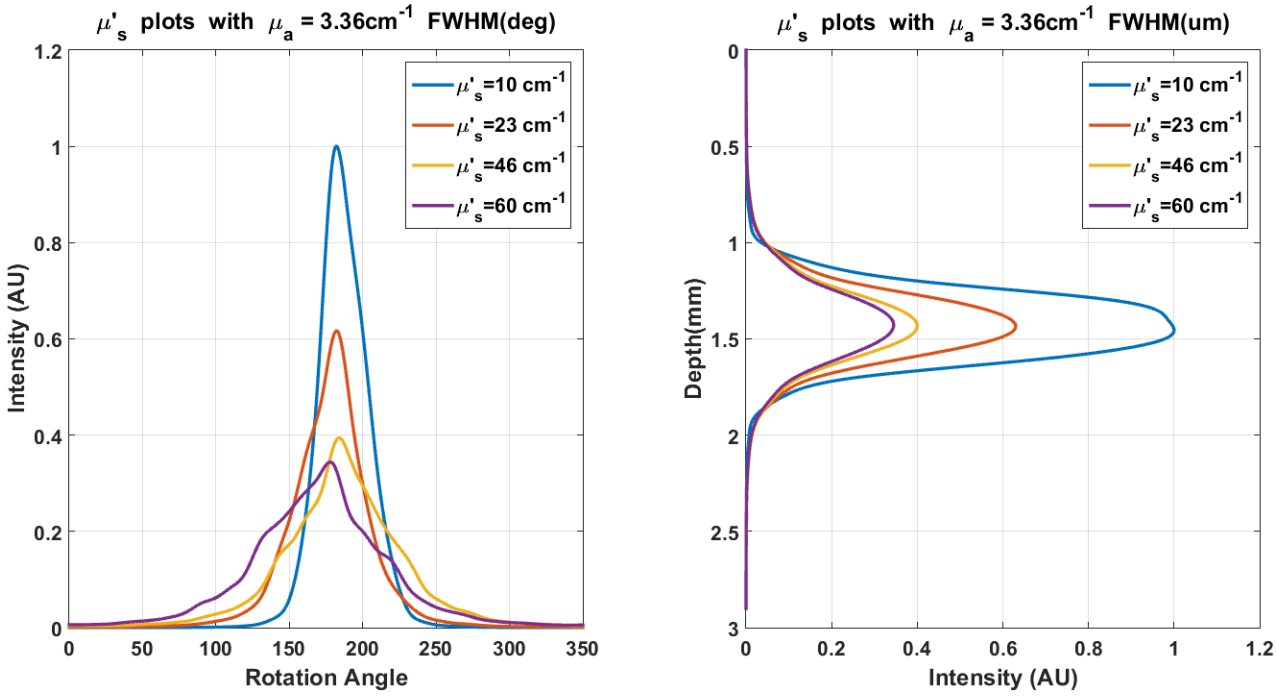

Figure 3.4 Effects of scattering on a simulated fluorescent microsphere. The left figure shows the strong effect of scattering which results in reduced peak intensity and a wider distribution. The fluorescent distribution does not show the same effects vertically. This is due to the resolution of 0.25mm used in the simulations.

A final consideration when running simulations was the change in NA. Figure 3.5 shows the simulation results for a varying NA from 0.2 to 0.6. The plot on the left represents the vertical FWHM in blue while the dashed red line represents the value for NA of 0.34 that we measured for our fiber. The plot on the right represents the radial FWHM. From these plots, we observe that as the NA increases, so does the FWHM. This is reasonable since rise in NA means that the acceptance angle gets larger. This accounts for more photons in the light cone.

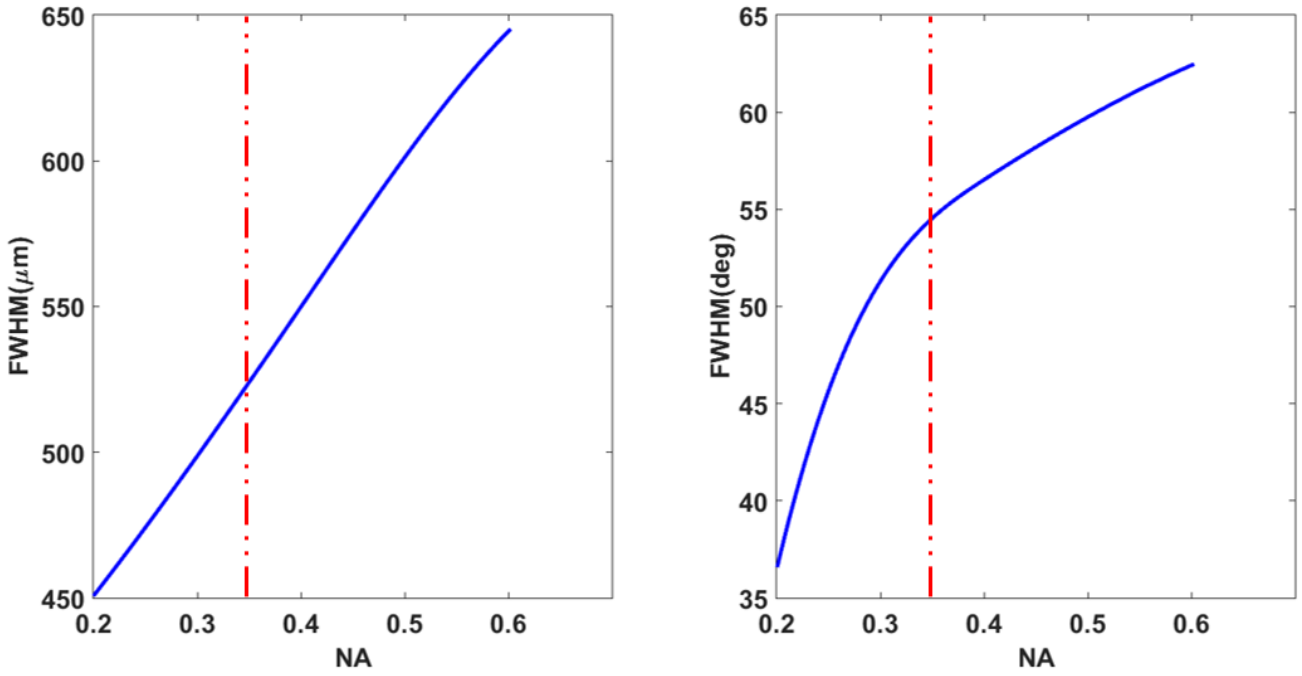

Figure 3.5 Plots of the effects from a varying NA on the FWHM for the fluorescent of a 250µm particle. Left plot shows the behavior of the FWHM vertically while right plot shows the behavior radially. The red lines represent the NA=0.34 which is the NA of the optical fiber in our system.

3.4 Phantom Experiments

To verify our system performance, we created a set of phantoms that have optical properties similar to the brain tissue. Biological tissue can vary from subject to subject and to this end, we observe the response of our system as calculated optical properties of brain tissue deviate from typical values. For our phantom creation, we used milk as a source of scattering and india ink as a source of absorption. With these concentrations and the use of fluorescent particles, we are able to experimentally recreate simulation setups.

3.4.1 Phantom Preparation and Set up

For phantom preparation, our first step was to choose a range of values from our simulations. We chose four values for μ_a (1,3,5,7 cm^{-1}) and four values for μ'_s (10, 26, 43, 60 cm^{-1}).

For our phantoms, we used 1% milk and then added ink in small concentrations to increase the absorbance of the phantom. Adding milk in small doses increases the scattering coefficient of the phantom. From previous literature, we find that an acceptable value of μ'_s is 22.5cm^{-1} for 1% milk [30]. The μ_a is typically very low ≈ .0035cm^{-1} [31].

The properties of india ink have been well documented and in the visible range, a typical value of μ_a is 3500cm^{-1}. The ink was diluted with water to obtain a μ_a = 35cm^{-1}. Due to the linear relationship between absorbance and concentration, we increased the absorption of our phantom by adding 0.1/(35*100ml) =.2857ml of india ink to a 100ml 1% milk to yield an absorption of ≈1cm^{-1} and scattering of 22.5cm^{-1}. Small doses of ink were added until absorption of the phantoms were 1,3,5, and 7 cm^{-1}.

Similarly, we can adjust the scattering by adjusting the concentration of milk by premixing milk and water before adding the absorber. For our phantoms that varied in μ'_s I mixed ratios of 1:3, 1:1, 5:3, and 33:7 milk to water concentrations to get μ'_s, of 10, 26, 43, 60cm^{-1} respectively.

Each mixture of liquid was made and a well array was used to test each of the concentrations. Figure 3.6 and Figure 3.7 show the concentrations as that are used to fill each well. Each well has a microsphere that is suspended in the liquid using a thin wire with a small amount of clear adhesive (Loctite).

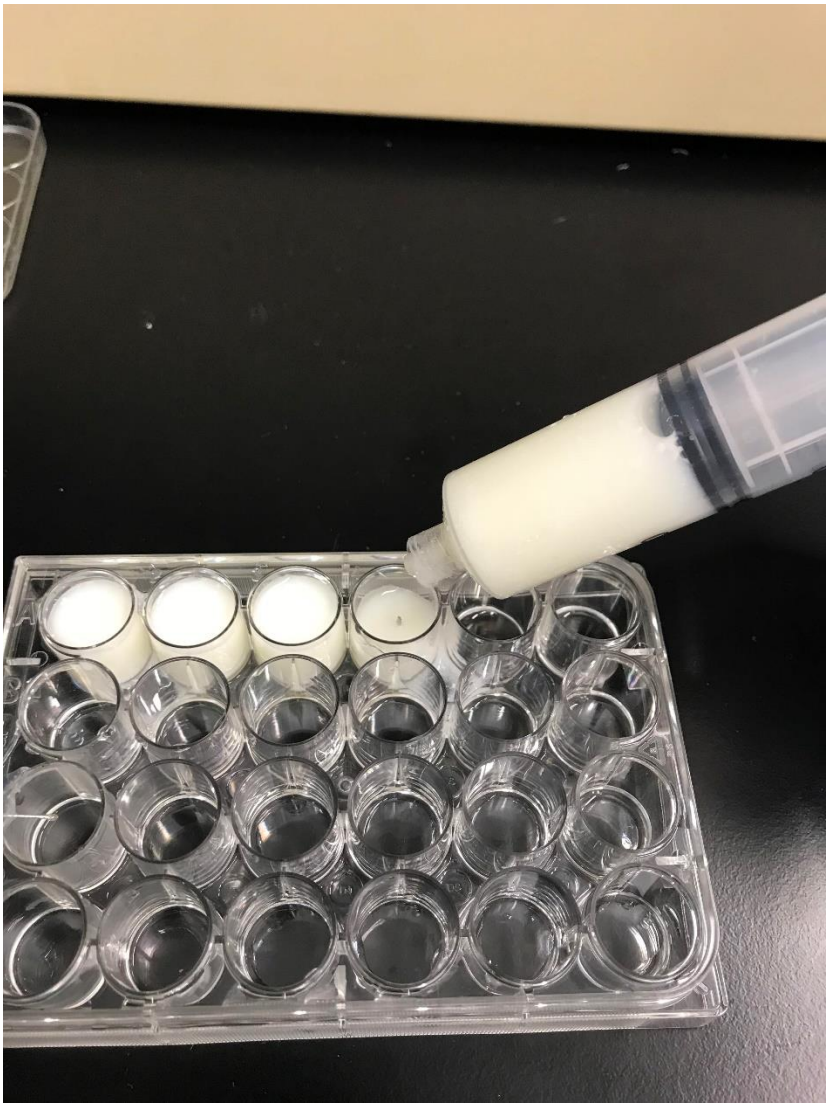

Figure 3.6 Picture of phantoms being made. Each well has a microsphere held in place with clear adhesive and a thin wire. Mixture of milk and water is added to the well to vary the scattering of the phantoms. Having a higher concentration of milk results in increased scattering.

Figure 3.7 Picture of absorber being added to an array of milk and water concentrations. India ink serves as an absorber that is added in different amounts to create liquid concentrations that have different absorptions.

The side firing fiber is then placed into the liquid .5mm away from a 250um fluorescent microsphere (Cospheric LLC) that has an excitation peak of 470nm close to the blue laser in our system and emission peak of 510nm which is also detectable by the EEDM. Figure 3.8 shows the fiber as it enters the milk concentration. The fiber travels into the liquid one step at a time and rotates and takes measurements of fluorescence.

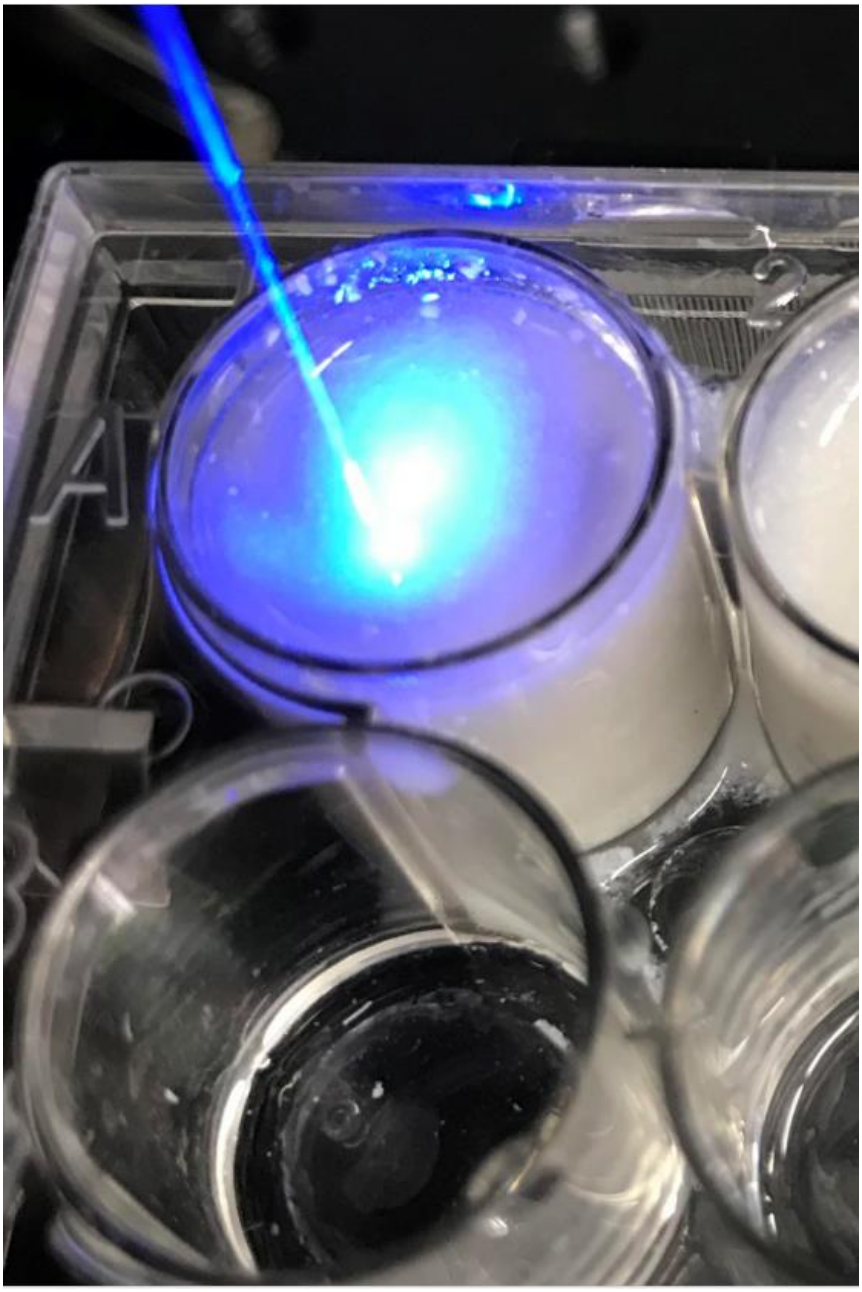

Figure 3.8 Picture of the side firing optical fiber as it enters the milk and ink mixture. The system scans through this liquid taking measurements as the fiber moves deeper into the phantom and rotates.

3.4.2 Phantom Results

Figure 3.9 and Figure 3.10 show the results of the phantom experiments where absorption changes. The effects of absorption can clearly be seen in the FWHM of the microsphere that is imaged. The figures on the left represent the collected data from our system and the images on the right is displaying the FWHM of the collected data. As the absorption increases, the FWHM decreases which is in accordance with our simulation results. From these images, we can focus on the area where there is highest fluorescence detected as the area of maximum light sensitivity.

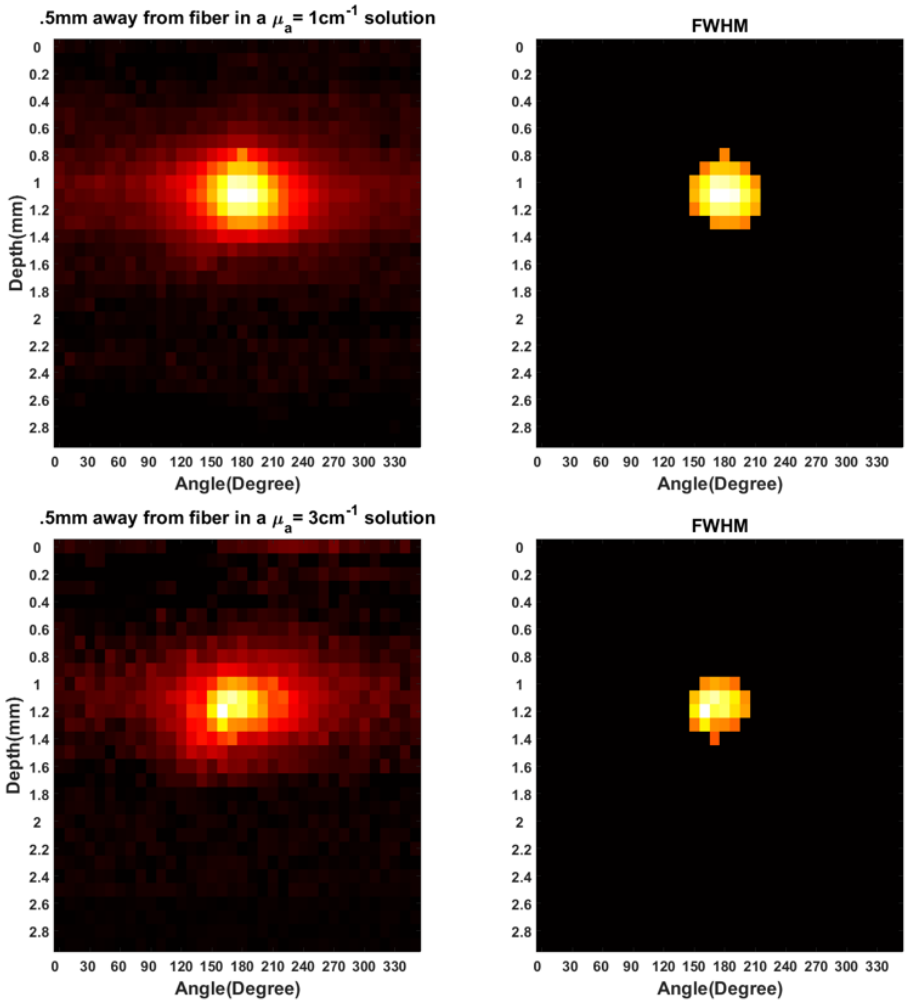

Figure 3.9 Captured images from phantom experiments for two different absorptions. Figures on the left are the full image and figures on the right show only the area within the FWHM of the fluorescence distribution.

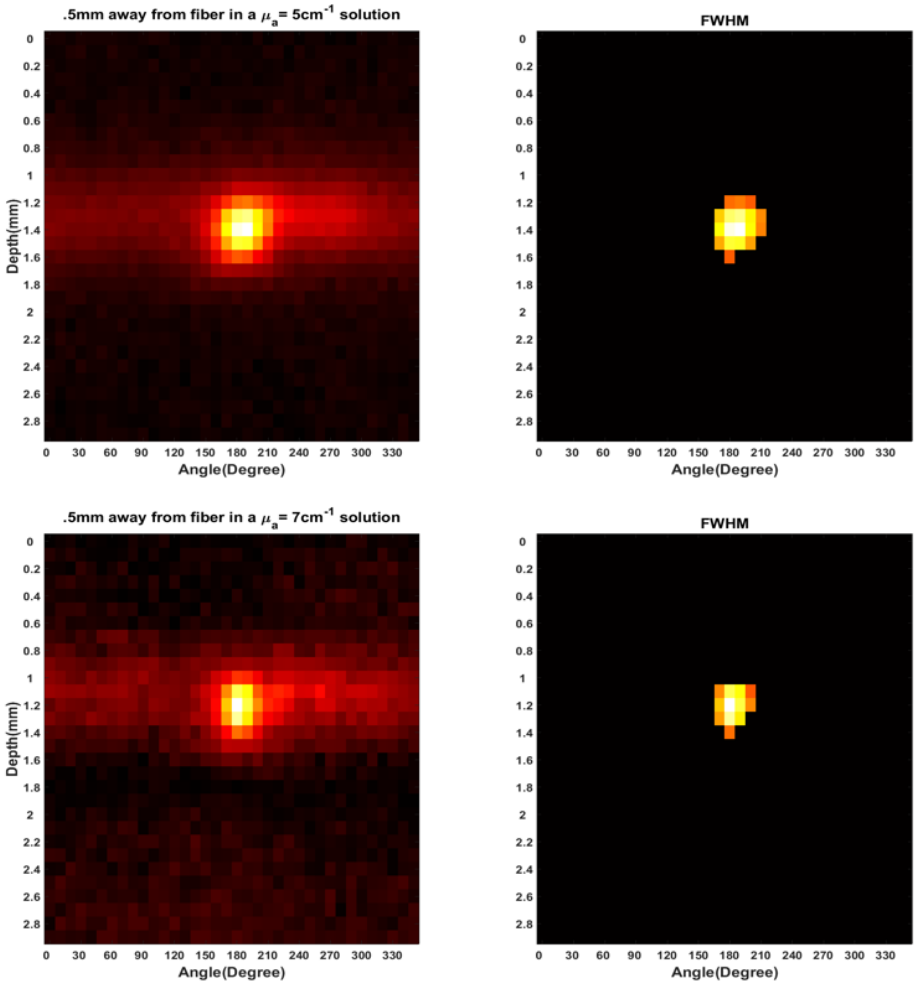

Figure 3.10 Captured images from phantom experiments for two absorptions. Figures on the left are the full image and figures on the right show only the area within the FWHM of the fluorescence distribution.

Figure 3.11 and Figure 3.12 show the results of the phantom experiments were μ'_s changes. The FWHM is increasing with the rise in the value of μ'_s. These results show a good relationship with our simulation results. The effects of higher milk concentration are displayed with wider distributions of fluorescence detected. The images on the left are the collected results from a 3mm vertical scan and the images on the right display FWHM of the collected data.

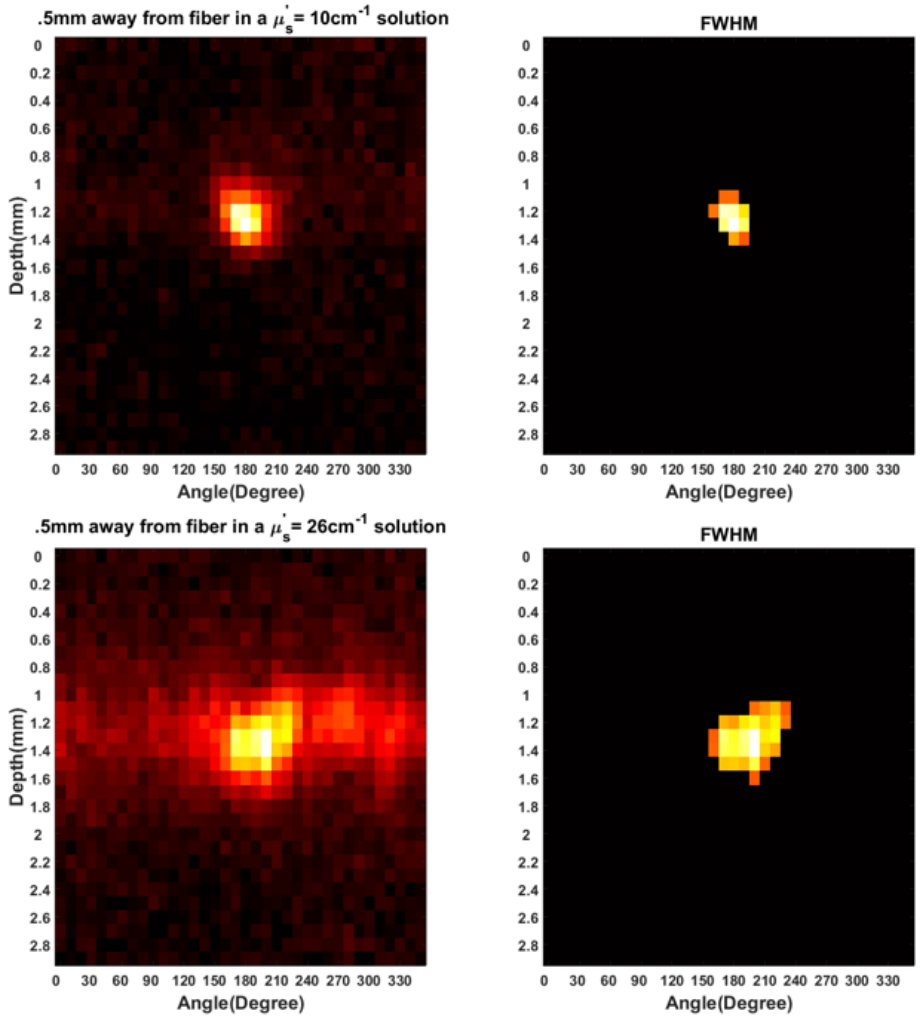

Figure 3.11 Captured images from phantom experiments for two values of μ'_s. Figures on the left are the full image from the collected data and figures on the right show only the area within the FWHM of the fluorescence distribution. The effects of higher scattering are clear from these images.

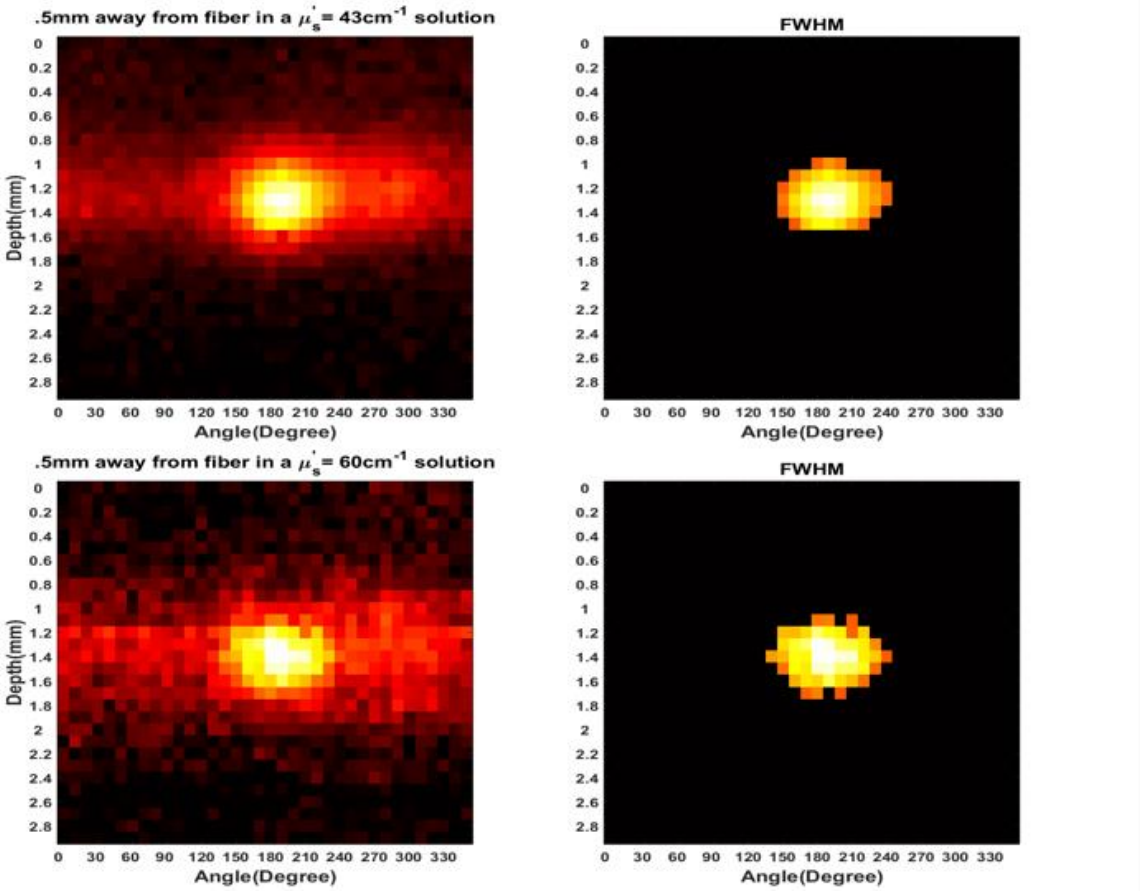

Figure 3.12 Captured images from phantom experiments for two μ'_s. Figures on the left are the full image and figures on the right show only the area within the FWHM of the fluorescence distribution.

In Figure 3.13 we compare all the results with the simulations. We see that the values of FWHM are within 20% of our simulations for the changing absorption. For the scattering, the results are within 25% of the simulated results which are still reasonable. One reason for the higher error in the scattering results is due to our original assumption that adding an absorber to the milk phantom would not change the scattering of the phantom because the absorption of ink is significantly higher. However, as the concentration of ink increases it can influence the scattering.

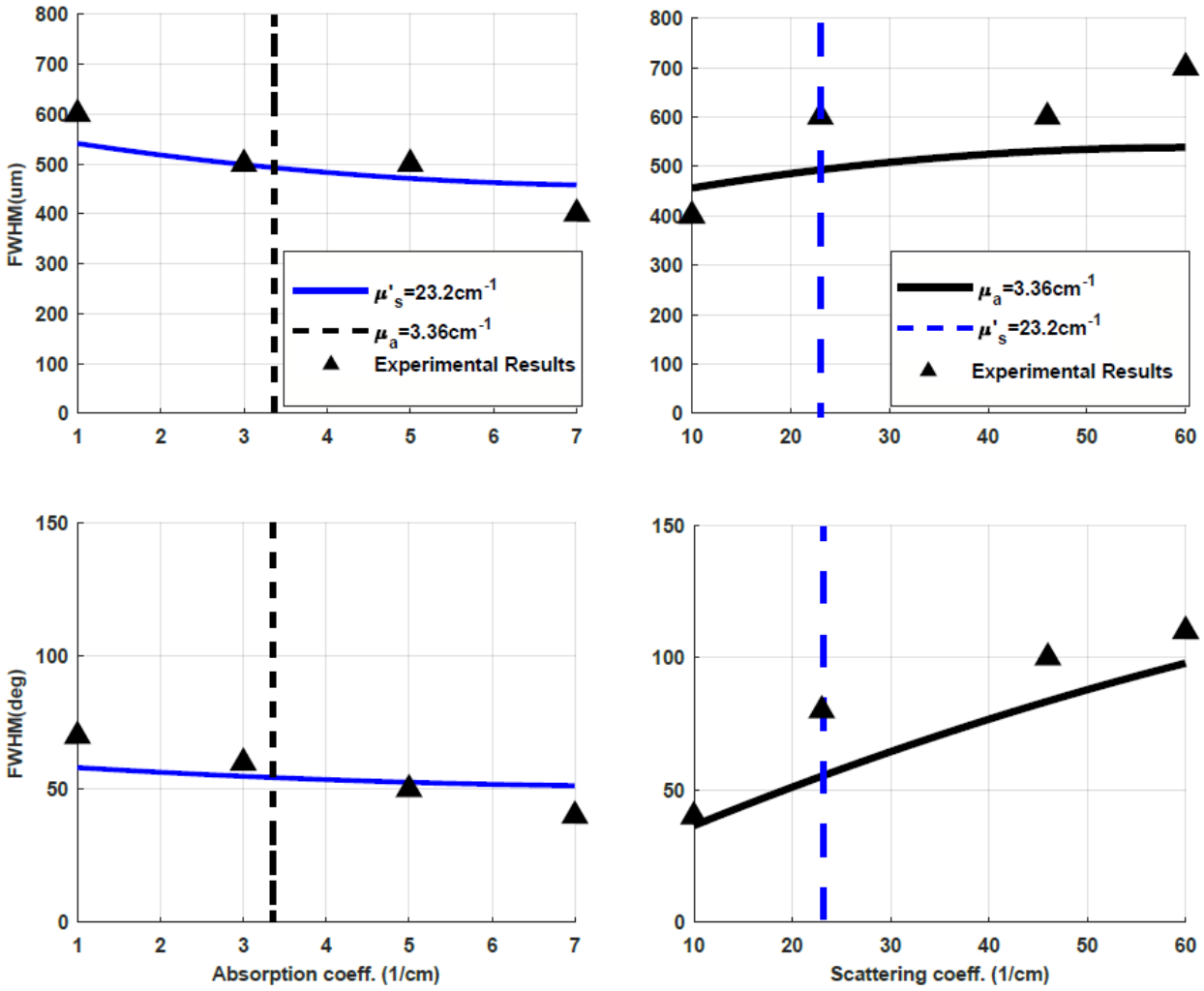

Figure 3.13 Results from phantom experiments compared to simulations. For μ_a, four data points are collected at 1,3,5,7cm^{-1} since our value for μ_a in brain tissue is 3.36cm^{-1}. Phantom results are within 20% of our simulations(Left). For the μ'_s, four data points at 10, 26, 43, 60cm^{-1} are collected. The value of μ'_s we used for simulations was 23.2cm^{-1}. These results are within 25% of the simulated values for FWHM.

3.5 Discussion

Simulations provide an intuition to the response of the system when making measurements in the tissue. Analyzing the results from the phantom experiments we expect the system to provide appropriate results in in-vivo experiments.

We still need to find the resolution for the system that is acceptable for our future in-vivo experiments. Using higher resolutions increases the accuracy of the system but it makes the

scanning process highly time consuming. For a scan with axial and radial resolutions of 100um and 10deg and taking two measurements for each pixel, the scan process can take up to 45min which is not reasonable. For this reason, we find the resolution of the system in both directions by simulating multiple fluorescent particles that are 0.5mm away from a side-firing optical fiber while changing the distance between them. Figure 3.14 shows four results. The top images show two particles 0.3 and 0.4mm apart and the bottom images show the microspheres 0.5 and 0.6mm apart from each other in the horizontal direction. It is clear from the figure that the particle will not be distinguishable from another when there is distance less than 0.5mm between them. This means that the rotation angle will have to be less than ≈50°. It is not surprising that the 50° is approximately the FWHM of one of these particles. However, 50° is still too large because in one 50° step one of these particles can be missed and therefore the limit is half of 50°. The scanning angle should not be more than 25°.

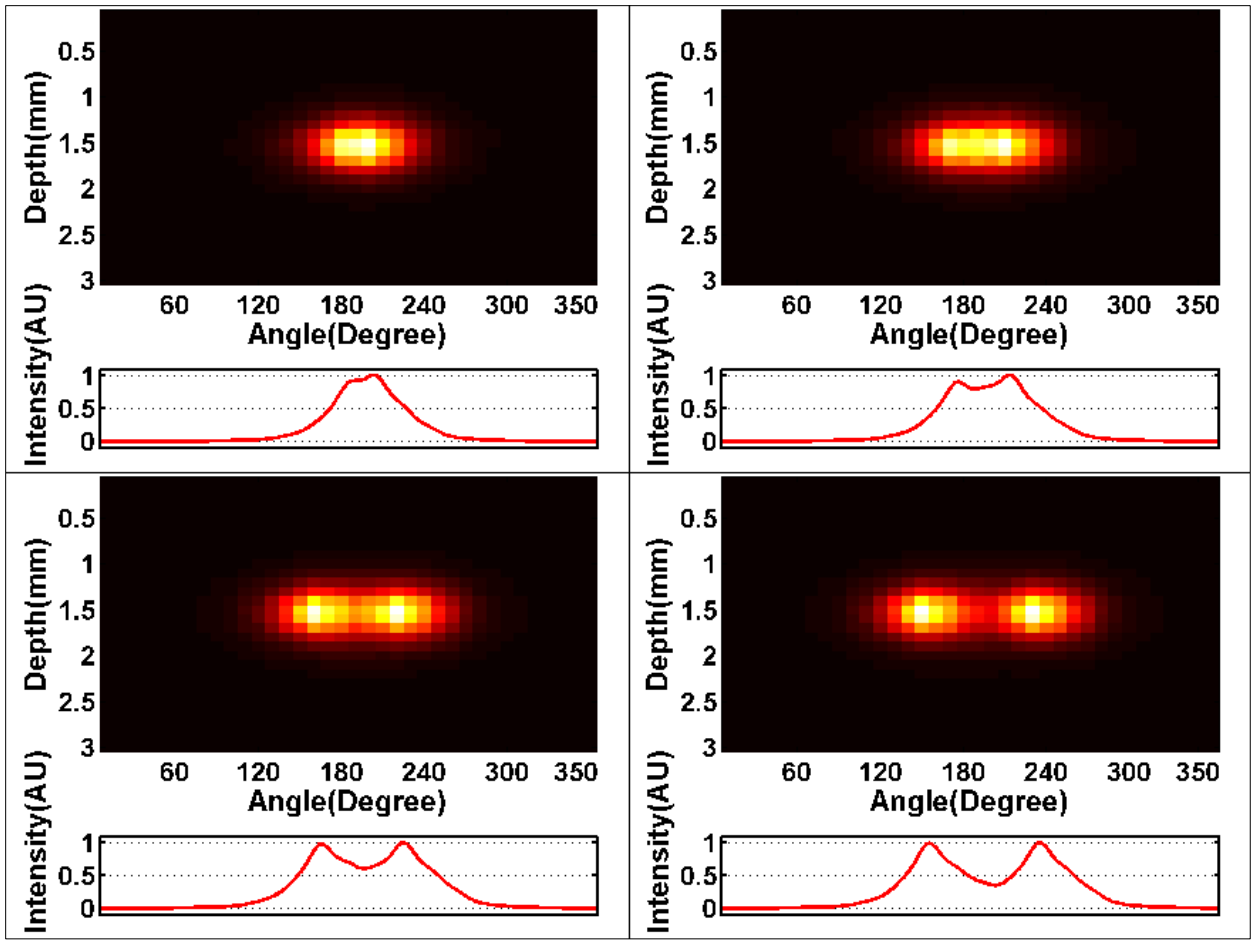

Figure 3.14 Results from a simulation to find the resolution of our proposed system. By moving two particles close to each other we see that at .5mm the particles become detectable as two different particles and the angle between them is ≈50°.

Figure 3.15 shows four results of the particles moving in the vertical direction. The top images show two particles 0.3 and 0.4mm apart and the bottom images show the microspheres 0.5 and 0.6mm apart from each other. It is clear from the figure that the particle will not be distinguishable from another when there is distance less than 0.49mm between them. Consequently, the vertical steps will have to be less than 0.49mm. Again, 0.49mm is still too large because in one vertical step of this size the particle can be missed. This results in a vertical step size that should not be more than 0.49/2 =0.245mm.

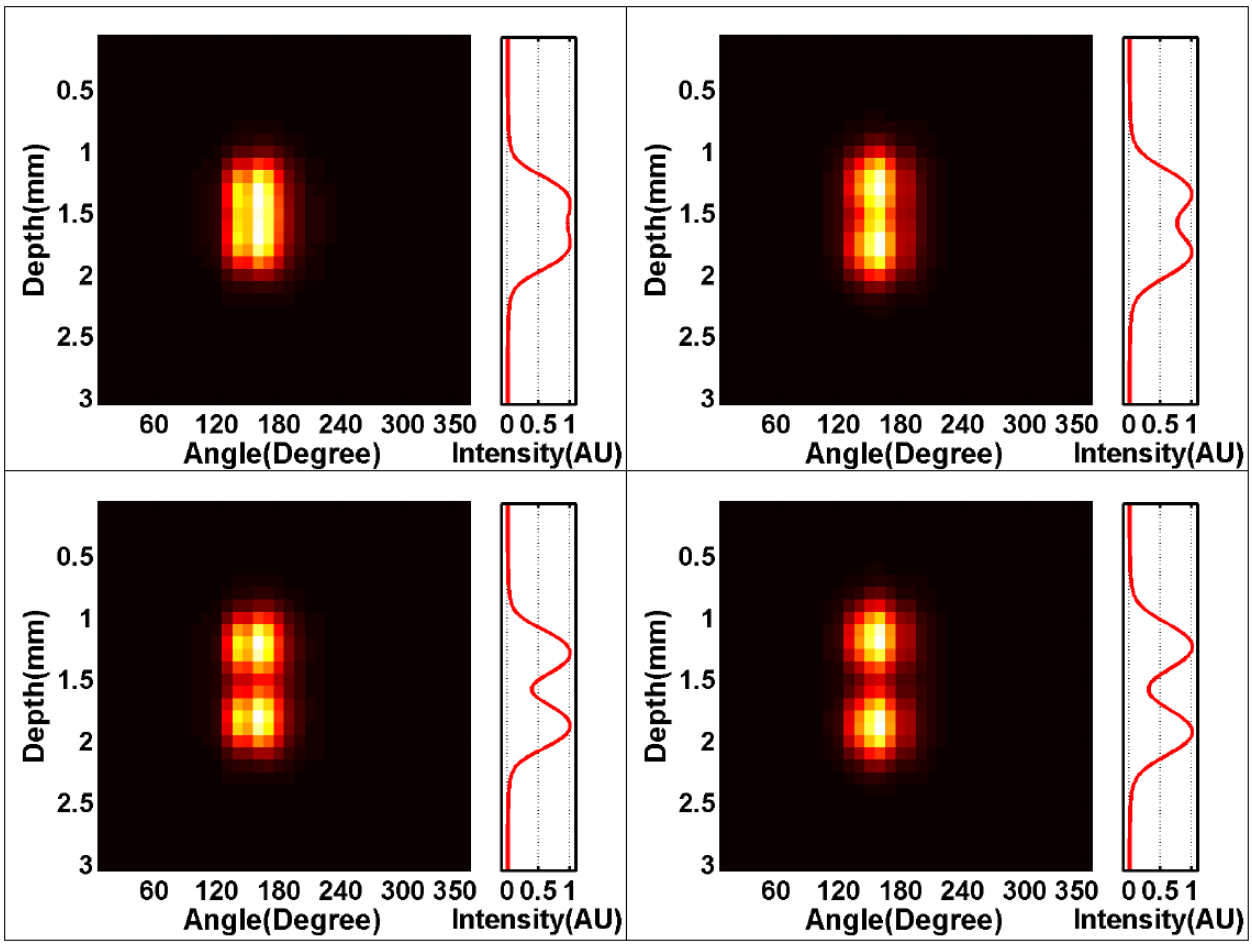

Figure 3.15 Results from a simulation to find the resolution of our proposed system. Images on the top are 0.3 and 0.4mm apart and images on the bottom are 0.5 and 0.6mm. By moving two particles close to each other in the vertical direction we see that at 0.49mm the particles become detectable as two different particles.

Another consideration is changing the wavelength of the system. By simulating multiple wavelengths, Figure 3.16, we see that as the wavelength increases, the resolution of the system is also affected. As the wavelength increases, the scattering decreases but so does the absorption. Since, the tissue does not absorb many photons, the smaller number of photons that do scatter affects the FWHM of an imaged particle and the resolution of the system.

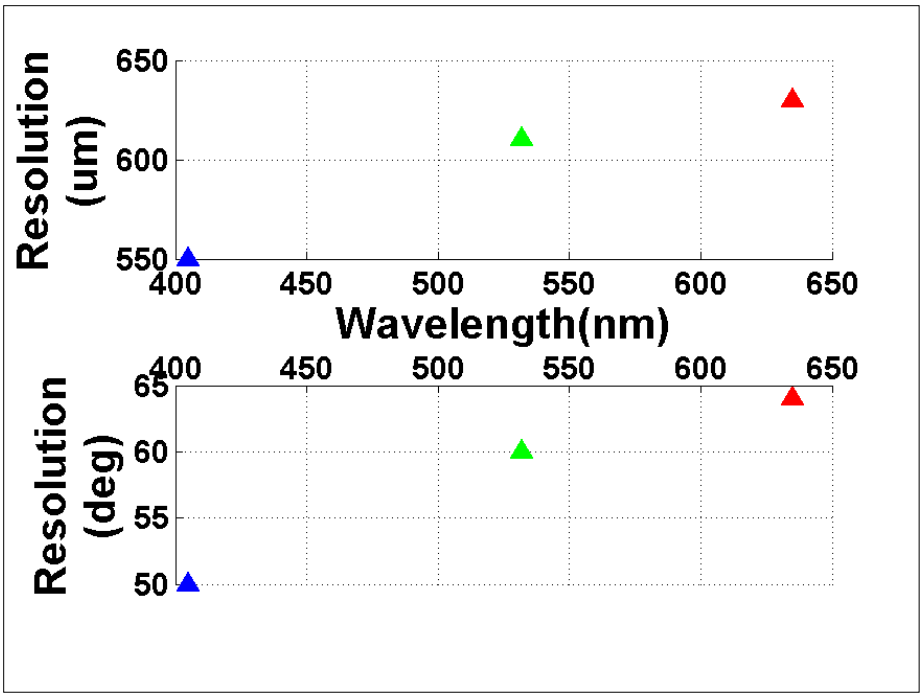

Figure 3.16 Results from spectral response simulations. Increasing wavelength influences the response of the proposed system. Resolution is in terms of FWHM. FWHM of a microsphere increases when the wavelength increases.

Chapter 4. Experimental Results

In this chapter, I will cover the results from in-vivo experiments. Figure 4.1 shows the experimental set up. For these experiments, a male Long-Evans rat (300-400g; Envigo, WI) housed in a shoebox cage with free access to food and water in a room maintained on a 14:10 light/dark cycle was used. All experiments took place during the light portion of the cycle. Spring-Fill Crinkle Cut Kraft paper (Quality Packaging, WI) paper bedding was provided as environmental enrichment. All procedures were carried out in a facility accredited by the Association for Assessment and Accreditation and Laboratory Animal Care and approved by the University of Wisconsin-Milwaukee Institutional Animal Care and Use Committee and conducted within the ethical guidelines of the National Institutes of Health.

Two weeks prior to experimentation, the animal was anesthetized with isoflurane in 100% oxygen (induction occurred with 4% isoflurane and maintained with 2%). Rat was mounted in a stereotaxic apparatus (Kopf Instruments). Purified AAV9-CAG-GFP was bilaterally infused into ventral hippocampus (A/P -5.28 mm, M/L + 5.4 mm, D/V 5.7 mm). The injection volume was 0.3µl. The virus was infused using a 10µl syringe with a 34-gauge needle mounted to a stereotaxic automated injector at a rate of 0.05 ul/min. The injector was left in place for 10 minutes following the injection to allow diffusion of the virus away from the injector.

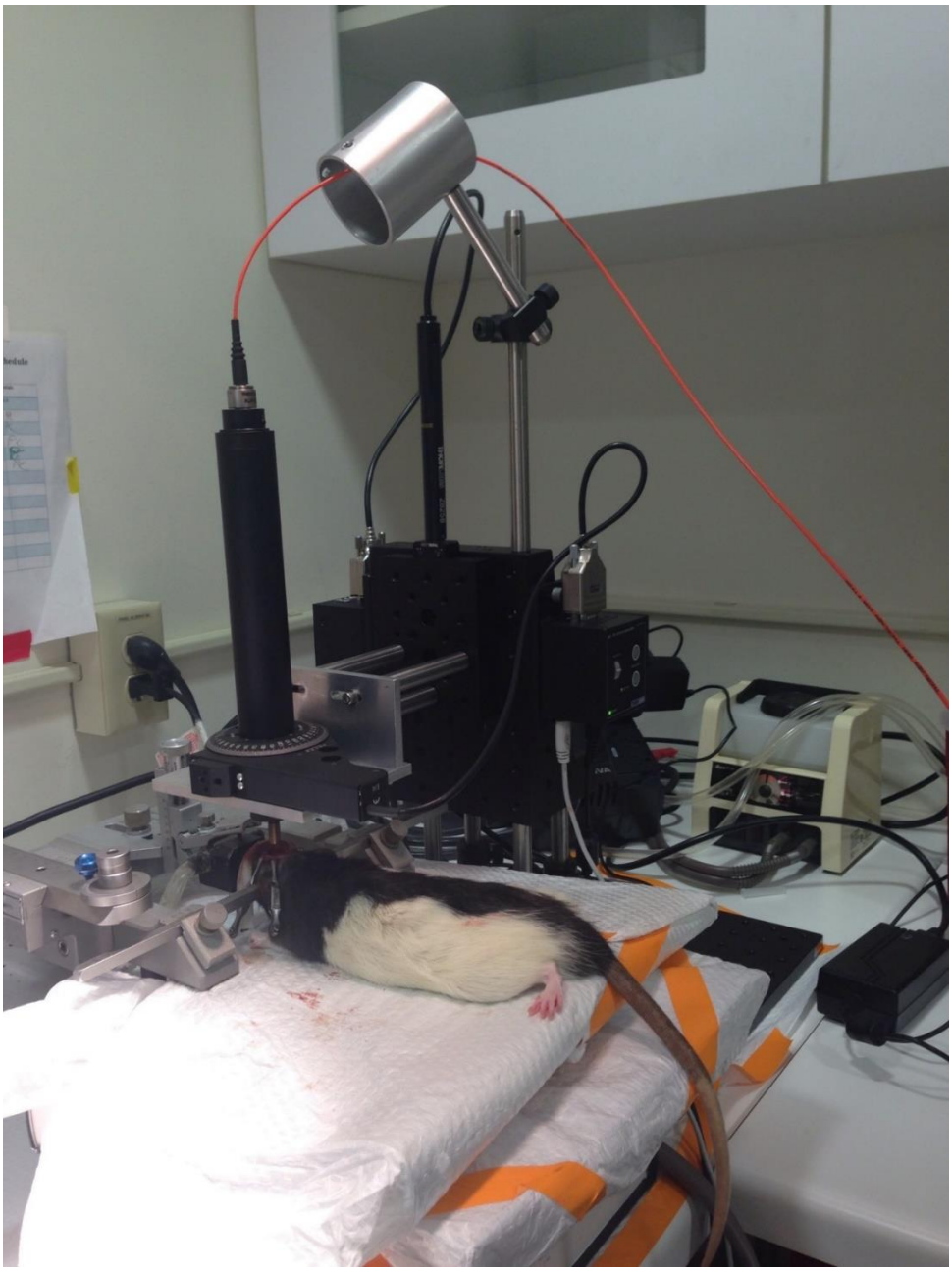

Figure 4.1 Experimental setup. Experiments were conducted in collaboration with the Neuroscience department at the University of Milwaukee-Wisconsin.

Immediately following the completion of the experiment, the animal was deeply anesthetized with isoflurane, transcardially perfused with 0.2M PBS followed by 10% buffered formalin. Brain was removed and post-fixed in 10% formalin for 24-hours before being transferred to 30%

sucrose/PB. The brain was then frozen, sectioned into coronal sections 200µm thick, mounted on glass slides, and cover slipped with UltraCruz mounting medium (Santa Cruz, CA) containing1.5µg/ml DAPI (for nuclear counter staining).

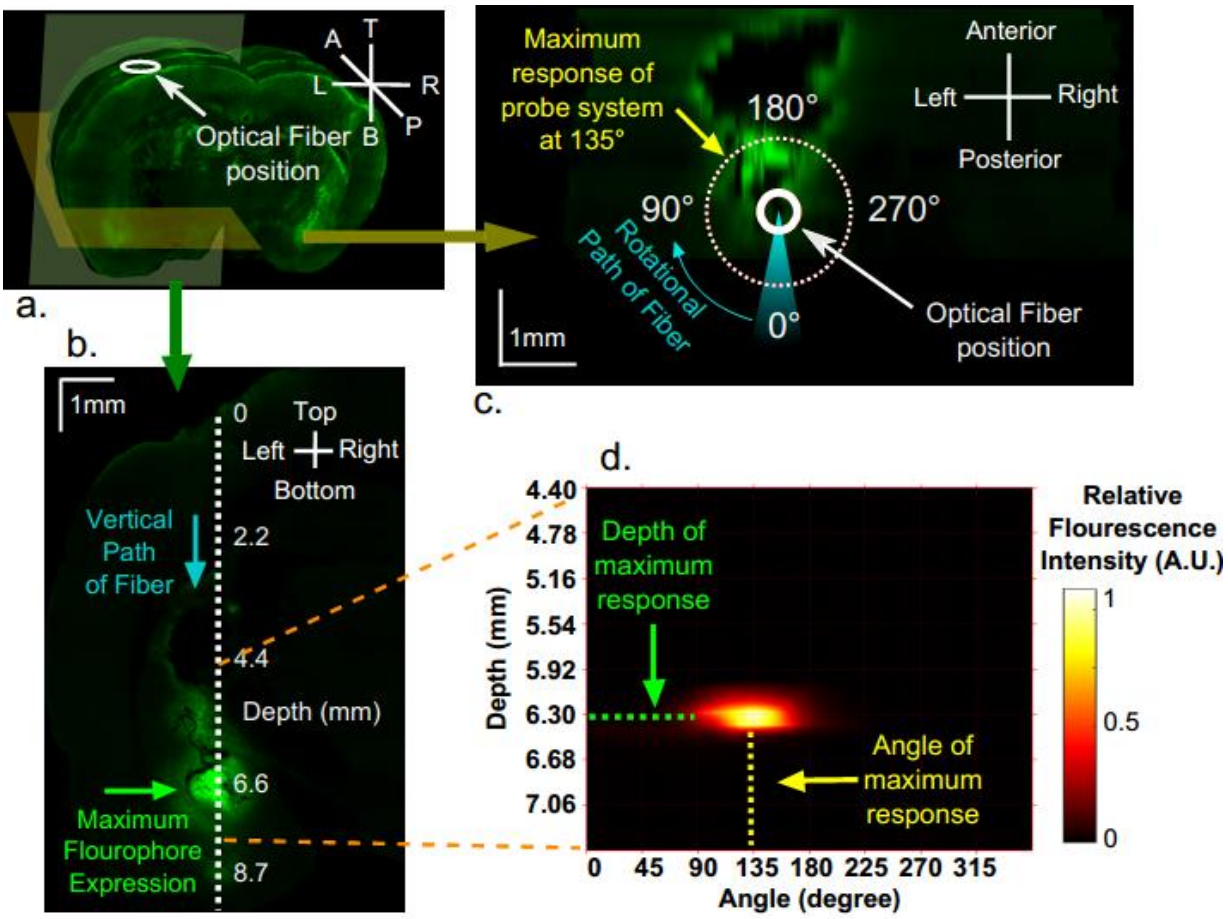

Figure 4.2 In-vivo results. 3D image reconstruction of a section from the brain(a). Following the path of the fiber maximum expression is shown at ≈6.6mm deep(b). Following the rotational path of the fiber there is maximum expression at the closest to the fiber at ≈135°(c). Data collected with our system and presented using gamma correction factor of 6 (d).

Measurements are mapped for each depth and for each angle with respect to the position of the fiber's main lobe of radiation. The data is presented after interpolating and processing using gamma correction with a gamma coefficient of 6.

After the experiment, the rat is euthanized and the brain is extracted. The brain is then sliced into 200um slices and each slice is imaged using a confocal microscope. Starting from a 3D reconstruction of a section of the brain shown in Figure 4.2 (a), we can find the exact location of the optical fiber entry point to the brain.

Two cross-sections are of interest to validate our results. The first, is a slice imaged by confocal microscopy shown in (b). The path of the optical fiber is marked on the image. Maximum fluorescence appears at approximately 800μm away from the fiber and 6.6mm deep. The measured data shown in (d) displays maximum intensity at 6.3mm deep in the brain. The difference in maximum expression at different depths is because the main lobe of radiation of the fiber is not completely orthogonal with the fibers optical axis. Taking the firing angle (73.81°) into account compensates for this discrepancy.

The second is the cross-section slicing the brain along the depth of maximum expression, shown in (c). The lobe of radiation is initially at 0º and as the fiber rotates clockwise collecting measurements every 20º, it detects the nearest distribution of fluorescence at 135º.

This agrees with our collected data which shows maximum expression at exactly 135º. While the distribution expands well into 180º of the initial position at 0º, the area of expression that is of nearest proximity to the optical fiber has the largest contribution to the measurement.

Chapter 5. Conclusion

It is important to consider the position of an optical fiber as well as direction of light delivery during optogenetic stimulation or other neuroscience experiments. The measured data clearly showed that the expression of fluorescence protein can diffuse in different directions with respect to the fibers main lobe of radiation. With the proposed system, we could accurately detect the depth and the orientation at which the maximum light sensitivity can be expected. This optimizes light delivery to successfully stimulate regions of the brain that have been genetically modified to express light sensitive proteins such as ChR2. While optogentics is only one application, the proposed system can be used in applications where the distribution of fluorescence needs to be imaged in soft tissue.

There are however limitations in this system that can be addressed in a future project. This project lacks any information about the radial depth of fluorescence distributions. This can be addressed by using multipoint-emitting optical fibers [32]. These fibers have multiple windows carved into them along their length. With the use of a fiber coupler and by adjusting the angle of input light, multiple windows can be used for stimulating or detection from different depths. With the use of an algorithm similar to that used in laminar optical tomography [13], we can potentially obtain radial depth information.

References

[1] S. L. Jacques, “Corrigendum: Optical properties of biological tissues: a review,” *Phys. Med. Biol.*, vol. 58, no. 14, pp. 5007–5008, 2013.

[2] K. L. Chou, S. Grube, and M. S. N. P. G. Patil, “A New Life for You,” p. 1.

[3] R. Pashaie and R. Falk, “Single optical fiber probe for fluorescence detection and optogenetic stimulation,” *IEEE Trans. Biomed. Eng.*, vol. 60, no. 2, pp. 268–280, 2013.

[4] R. Pashaie *et al.*, “Optogenetic brain interfaces,” *IEEE Rev. Biomed. Eng.*, vol. 7, pp. 3–30, 2014.

[5] R. J. Mallia, “Photodiagnosis of Oral Malignancy using Laser-Induced Fluorescence and Diffuse Reflectance Spectroscopy,” Cochin University of Science and Technology, 2008.

[6] V. Tuchin, *Tissue Optics: Light Scattering Methods and Instruments for Medical Diagnosis, Second Edition*. SPIE Press Monograph, 2007.

[7] “Wikipedia.” [Online]. Available: https//www.wikipedia.org. [Accessed: 01-Nov-2017].

[8] J. W. Pickering, S. A. Prahl, N. van Wieringen, J. F. Beek, H. J. C. M. Sterenborg, and M. J. C. van Gemert, “Double-integrating-sphere system for measuring the optical properties of tissue,” *Appl. Opt.*, vol. 32, no. 4, p. 399, 1993.

[9] M. W. Abramowitz, Mortimer; Davidson, “Fluorescence: overview of excitation and emission fundamentals.” [Online]. Available: https://micro.magnet.fsu.edu/primer/lightandcolor/fluoroexcitation.html. [Accessed: 01-Nov-2017].

[10] M. Sundberg, “Optical Methods for Tympanic Membrane Characterisation : Towards

Objective Otoscopy in Otitis Media," Linköping University, 2008.

[11] A. P. Dhawan, H. K. Huang, and D.-S. Kim, *Principles and Advanced Methods in Medical Imaging and Image Analysis*. 2008.

[12] "Mecanusa." [Online]. Available: http://www.mecanusa.com.

[13] M. Azimipour *et al.*, "Fluorescence laminar optical tomography for brain imaging: system implementation and performance evaluation," *J. Biomed. Opt.*, vol. 22, no. 1, 2017.

[14] L. V Wang and H. Wu, *Biomedical optics : principles and imaging*. Hoboken, N.J.: Wiley-Interscience, 2007.

[15] M. R. Shirkavand, Afshan & Sarkar, Saeed & Hejazi, Marjaneh & Ataie-Fashtami, Leila & Alinaghizadeh, "A new Monte Carlo code for absorption simulation of laser-skin tissue interaction," *Chinese Opt. Lett.*, pp. 238–240, 2007.

[16] C. Zhu and Q. Liu, "Review of Monte Carlo modeling of light transport in tissues," *J. Biomed. Opt.*, vol. 18, no. 5, p. 50902, 2013.

[17] S. L. Jacques and L. Wang, *"Monte carlo modeling of light transport in tissues". In Optical Thermal Response of Laser-Irradiated Tissue*. New York: Plenum Press, 1995.

[18] F. Zhang, A. M. Aravanis, A. Adamantidis, L. De Lecea, and K. Deisseroth, "Circuit-breakers: Optical technologies for probing neural signals and systems," *Nat. Rev. Neurosci.*, vol. 8, no. 8, pp. 577–581, 2007.

[19] F. Zhang *et al.*, "Multimodal fast optical interrogation of neural circuitry," *Nature*, vol. 446, no. 7136, pp. 633–639, Apr. 2007.

[20] A. B. McElrone, "Edible Neuron Diagram." [Online]. Available: https://www.education.com/science-fair/article/edible-neuron-diagram/.

[21] M. F. Bear, B. W. Connors, and M. A. Paradiso, *Neuroscience: Exploring the Brain*. Philadelphia, PA: Lippincott Williams Wilkins, 2007.

[22] M. Sheikhzadeh, "Design , Implementation , and Evaluation of a Fluorescence Laminar Optical Tomography Scanner for Brain Imaging Scanner for Brain Imaging," University of Wisconsin Milwaukee, 2016.

[23] T. Knopfel, M. Z. Lin, A. Levskaya, L. Tian, J. Y. Lin, and E. S. Boyden, "Toward the Second Generation of Optogenetic Tools," *J. Neurosci.*, vol. 30, no. 45, pp. 14998–15004, 2010.

[24] M. E. Carter and L. de Lecea, "Optogenetic investigation of neural circuits in vivo," *Trends Mol. Med.*, vol. 17, no. 4, pp. 197–206, 2011.

[25] M. A. Richards, *Fundamentals of Radar Signal Processing*. New York: McGraw Hill, 2005.

[26] R. George and L. J. Walsh, "Performance assessment of novel side firing flexible optical fibers for dental applications," *Lasers Surg. Med.*, vol. 41, no. 3, pp. 214–221, 2009.

[27] F. Wezel *et al.*, "New alternatives for laser vaporization of the prostate: Experimental evaluation of a 980-, 1,318- and 1,470-nm diode laser device," *World J. Urol.*, vol. 28, no. 2, pp. 181–186, 2010.

[28] Y. Liu, S. L. Jacques, M. Azimipour, J. D. Rogers, R. Pashaie, and K. W. Eliceiri, "OptogenSIM: a 3D Monte Carlo simulation platform for light delivery design in optogenetics," *Biomed. Opt. Express*, vol. 6, no. 12, p. 4859, 2015.

[29] S. L. Prahl, S. A. ;Jacques, "Monte Carlo simulations." [Online]. Available: http://omlc.org/software/mc/. [Accessed: 06-Jan-2016].

[30] M. Azimipour, R. Baumgartner, Y. Liu, S. L. Jacques, K. Eliceiri, and R. Pashaie, "Extraction of optical properties and prediction of light distribution in rat brain tissue," *J. Biomed. Opt.*, vol. 19, no. 7, p. 75001, 2014.

[31] J. Gwamuri, A. V Gholap, T. S. M. Shartir, and P. K. Bauh-Bassuah, "Investigating Light Propagation In Turbid Media By Evaluating Optical Properties Of Phantom Tissues," *Sponsors*, no. November, p. 55, 2006.

[32] F. Pisanello *et al.*, "Multipoint-emitting optical fibers for spatially addressable in vivo optogenetics," *Neuron*, vol. 82, no. 6, pp. 1245–1254, 2014.